A magnetotelluric investigation of the Scandinavian Caledonides in western Jämtland, Sweden, using the COSC borehole logs as prior information

Ping Yan,[1] Maria A. Garcia Juanatey,[1] Thomas Kalscheuer,[1] Christopher Juhlin,[1] Peter Hedin,[1] Alexandros Savvaidis,[2] Henning Lorenz[1] and Jochem Kück[3]

[1]*Department of Earth Sciences, Uppsala University, Uppsala, Sweden. E-mail:* yan.ping@geo.uu.se
[2]*Bureau of Economic Geology, Jackson School of Geoscience, University of Texas at Austin, TX, USA*
[3]*Centre for Scientific Drilling, Helmholtz Centre Potsdam, GFZ German Research Centre for Geosciences, Germany*

SUMMARY

In connection with the Collisional Orogeny in the Scandinavian Caledonides (COSC) project, broad-band magnetotelluric (MT) data were acquired at 78 stations along a recent *ca*. 55-km-long NW–SE directed reflection seismic profile (referred to as the COSC Seismic Profile; CSP), with the eastern end located ∼30 km to the west of the orogenic Caledonian front. The MT component of the project aims at (i) delineating the highly conductive (∼0.1 Ω · m) alum shales that are associated with an underlying main décollement and (ii) calibrating the MT model to borehole logs. Strike and distortion analyses of the MT data show a 3-D structure in the western 10 km of the profile around the 2.5 km deep COSC-1 borehole (IGSN: ICDP5054EHW1001) and a preferred strike angle of N34°E in the central and eastern parts of the profile. 2-D modelling of MT impedances was tested using different inversion schemes and parameters. To adjust the resistivity structure locally around the borehole, resistivity logging data from COSC-1 were successfully employed as prior constraints in the 2-D MT inversions. Compared with the CSP, the model inverted from the determinant impedances shows the highest level of structural similarity. A shallow resistor (>1000 Ω · m) in the top 2–3 km depth underneath the western most 10 km of the profile around COSC-1 corresponds to a zone of high seismic reflectivity, and a boundary at less than 1 km depth where the resistivity decreases rapidly from >100 to <1 Ω · m in the central and eastern parts of the profile coincides with the first seismic reflections. The depth to this boundary is well constrained as shown by 1-D inversions of the MT data from five selected sites and it decreases towards the Caledonian front in the east. Underneath the easternmost part of the profile, the MT data show evidence of a second deeper conductor (resistivity <1 Ω · m) at >3 km depth. Based upon the COSC-1 borehole logs, the CSP reflection seismic image, and the surface geologic map, the MT resistivity models were interpreted geologically. In the vicinity of COSC-1, the resistor down to 2–3 km depth pertains to the metamorphic Middle Allochthon. The up to 1000-m-thick shallow resistor in the central and eastern parts of the profile is interpreted to overly an imbricated unit at the bottom of the Lower Allochthon that includes the alum shales. In the MT resistivity model, the 300–500 m thick imbricated unit masks the main Caledonian décollement at its bottom. A second possible interpretation, though not favoured here, is that the décollement occurs along a much deeper seismic reflection shallowing from 4.5 km depth in the west to ∼600 m depth in the east. An additional borehole (COSC-2) is planned to penetrate the Lower Allochthon and the main décollement surface in the central part of the profile and can provide information to overcome this interpretational ambiguity. Using a synthetic study, we evaluate how resistivity logs from COSC-2 can improve the 2-D inversion model.

Key words: Inverse theory; Downhole methods; Magnetotellurics; Continental tectonics: compressional; Europe.

1 INTRODUCTION

As one of the world's major mid-Palaeozoic mountain belts, the Scandinavian Caledonides offer unique opportunities to study a Himalayan-type orogeny given that the lateral transport of Caledonian allochthons over distances of over 400 km is similar to that recognized in the Himalayas (Dewey 1969). The Collisional Orogeny in the Scandinavian Caledonides (COSC) scientific continental drilling project was designed to focus on Mid-Palaeozoic mountain building processes in western Scandinavia (Lorenz *et al.* 2011, 2015a,b). With two fully cored boreholes (COSC-1, drilled in 2014 May–August; COSC-2, in the planning phase), each to ~2.5 km depth, the COSC project aims to investigate both the Caledonian nappes and the underlying basement to further our current understanding of orogenic processes (Gee *et al.* 2010). Additionally, various geophysical investigations have been included within the COSC project. These include an MT survey along a 60-km-long profile conducted in 2013. MT is expected to be a very useful method for delineating the top of the highly conductive alum shales, which are associated with the décollement zone between the Caledonian allochthons and the underlying Precambrian basement. The effectiveness of electromagnetic (EM) mapping of conductive alum shale was first demonstrated in the county of Västerbotten in the early 1960s (Gee 1972) and later confirmed, among others, by Korja *et al.*'s (2008) study.

In this paper, besides state-of-the-art MT processing and inversion, an algorithm for using the borehole logging data as prior constraints in the 2-D MT inversion is proposed, as two types of borehole resistivity logs (short and long normal resistivity logs and shallow and deep laterologs) are available in COSC-1 and more resistivity logging data will be collected in COSC-2. Based on our investigations, the inversion model constrained by the deep laterolog data was chosen as the final model. This final model was interpreted taking into account information from the COSC-1 borehole logs, a reflection seismic section, a surface geologic map and airborne VLF data.

1.1 Geological setting

After the Iapetus Ocean between Baltica and Laurentia was closed in the Early Silurian, the Scandinavian Caledonides were formed through the underthrusting of continent Laurentia by Baltica and the subsequent collisional orogeny during the Early Devonian period (Gee *et al.* 2008). The structure of the Scandinavian Caledonides is dominated by a variety of thrust sheets that were emplaced from west to east onto the Baltoscandian Platform and have small vertical thickness and wide lateral extent. W-to-NW-directed extensional faulting and folding resulted in depressions and culminations in the basement (Fig. 1; Corfu *et al.* 2014). A detailed review of the Scandinavian Caledonides, including regional reviews, structure, igneous activity, metamorphism and tectonic evolution, is presented by Gee & Sturt (1985). The main features and the major scientific discoveries in the last three decades were summarized by Corfu *et al.* (2014). In the present summary, we focus on the area from Åre to Östersund in western Jämtland (yellow square in Figs 1 and 2), where we collected MT data. The detailed geology of this area has been previously described by Gee *et al.* (2010), Hedin *et al.* (2012, 2014) and Juhlin *et al.* (2016).

The Caledonian allochthons were folded into major N–S-trending synforms and antiforms with tens of kilometres wavelengths, possibly above a deeper seated sole thrust in the Baltican basement (Fig. 1). In western Jämtland, the N-trending Åre Synform is flanked by the Mullfjället Antiform in the west and by the Olden-Oviksfjäll Antiform in the east (Fig. 2). In the study area, a slightly westwards dipping detachment separates the Caledonian nappes from the underlying Proterozoic basement of the Fennoscandian Shield, consisting mainly of granites, gneisses, porphyrites, migmatites and volcanic rocks. The nappes in the study area belong to two major tectonic units called the Lower and Middle Allochthons and contain mainly sedimentary and metamorphic rocks from the passive continental margin of Baltica (Fig. 2; Gee *et al.* 1985).

The Lower Allochthon includes Cambrian black alum shales, overlain by Ordovician limestones and Ordovician to Silurian greywackes (turbidites). At the Caledonian front (Fig. 1), shallow drilling has shown that Ordovician limestones, black shales and, occasionally, quartzites from the thin basement cover below the detachment are intercalated along the detachment horizon that is hosted by the alum shales (Andersson *et al.* 1985).

The Middle Allochthon is characterized by a higher metamorphic grade and is usually separated from the Lower Allochthon by a several meters thick zone of mylonites and phyllonites. In general, the Middle Allochthon is readily divisible into two parts: a lower part and the Seve Nappe Complex. The lower part of the Middle Allochthon is composed of three tectonic units: a main basement-derived thrust sheet at the bottom which is, in general, extensively mylonitized and retrogressed, overlain by the Offerdal Nappe which is dominated by feldspathic psammites, and at the top the Särv Nappe with metasandstones intersected by abundant dolerite dyke-swarms. Overlying the Särv Nappe is the Seve Nappe Complex, which largely consists of amphibolites, psammitic schists, gneisses and migmatites and probably was derived from the outer to outermost continental margin of Baltica, including the continent-ocean transition zone (Gee *et al.* 1985). In Jämtland, the Seve Nappe Complex is known to consist of three units, where the Lower Seve Nappe is similar to the underlying Särv Nappe, with psammitic schists and amphibolites, but deformed in amphibolite facies. This is overlain by the Åreskutan Nappe (and comparable units), which consists of gneisses, granulites and migmatites with evidence for ultra-high pressure metamorphism (Majka *et al.* 2014; Klonowska *et al.* 2015). The upper unit is dominated by garnet micaschists and amphibolites (Gee *et al.* 1985, 2010).

1.2 Previous geophysical studies

In western Jämtland, petrophysical sampling (Elming 1980), potential field surveys (Dyrelius 1980, 1986), seismic refraction (Palm 1984) and MT (Agustsson 1986) were conducted in the mid-1980s as a part of the Swedish contribution to the International Geodynamics Project (Bylund *et al.* 1976) to study crustal structures. Between 1988 and 1992, a 250-km-long reflection seismic survey was carried out along the Central Caledonian Transect (CCT, dashed yellow line in Fig. 2) to study the entire crust down to the Moho (Hurich *et al.* 1989; Juhojuntti *et al.* 2001; Palm *et al.* 1991). The CCT seismic profile revealed the crust to be 40–50 km thick in the Jämtland area, with strong laterally continuous zones of reflections in the uppermost 20 km and transparent zones in the lower crust. The uppermost reflections correlate well with the surface geology, and a gently westward-dipping reflection was detected that can be traced from the surface at the orogenic front in central Jämtland to the Swedish-Norwegian border where it reaches a depth of ~7 km. This westward-dipping reflection, although not continuous, was interpreted as a detachment surface (Palm *et al.* 1991). Korja *et al.* (2008) deployed 60 broadband magnetotelluric (MT) stations along the CCT reflection seismic profile in western Jämtland (note that
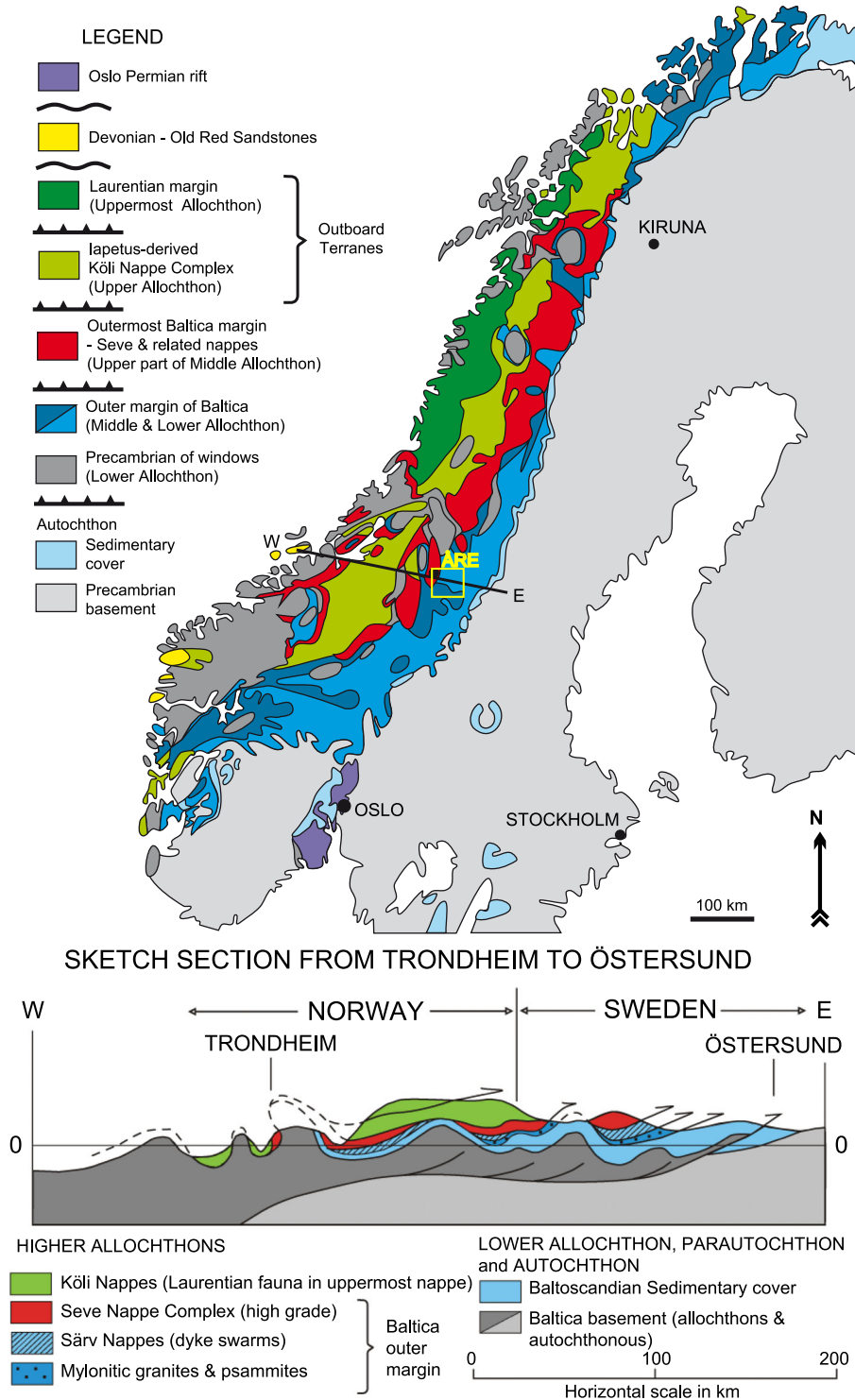
Figure 1. Geological map of Scandinavian Orogeny and cross-section through the Central Scandes between points W and E (modified after Gee *et al*. 2010). Our measurement area at Åre is marked with a yellow rectangle.

only 7 MT stations are in the area plotted in Fig. 2 and are marked as green diamonds). The MT inversion model showed a highly conductive layer with a well-defined upper boundary underlying a resistive layer. The boundary, which projected to the surface at the Caledonian front, coincided with strong reflections in the CCT reflection seismic section and was interpreted as the main décollement which separates the Precambrian basement from the Caledonian

allochthons and is associated with highly conductive alum shales (Gee and Sturt, 1985).

The apparent resistivity of airborne very low frequency (VLF; 15–30 kHz) data (Becken & Pedersen 2003), collected in the study area by the Geological Survey of Sweden (SGU), is presented in Fig. 3. The VLF method is a useful EM tool for mapping near-surface structures in the uppermost hundred meters (McNeill &
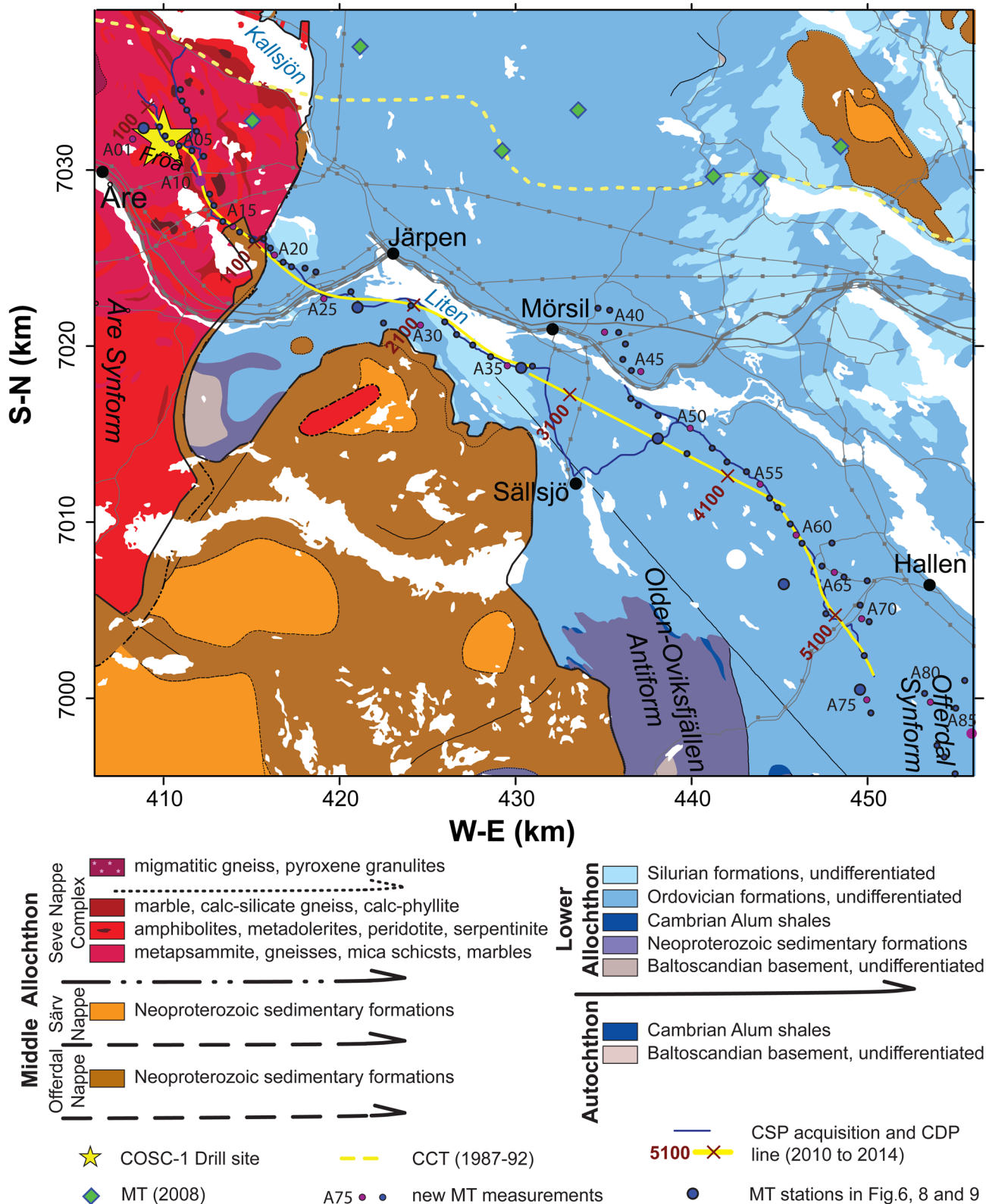
Figure 2. Geologic map of the study area with locations of new broad-band MT stations (blue and purple dots), borehole COSC-1 (yellow star, Lorenz *et al.* 2015a,b), previous MT stations (green diamonds, Korja *et al.* 2008), recent reflection seismics along CSP (continuous yellow lines; Hedin *et al.* 2012; Juhlin *et al.* 2016) and previous reflection seismics along the CCT profile (dashed yellow line, Juhojuntti *et al.* 2001). Based on the bedrock geological map of Sweden, © Geological Survey of Sweden [I2014/00601] and Strömberg *et al.* (1984), and modified after Juhlin *et al.* (2016).
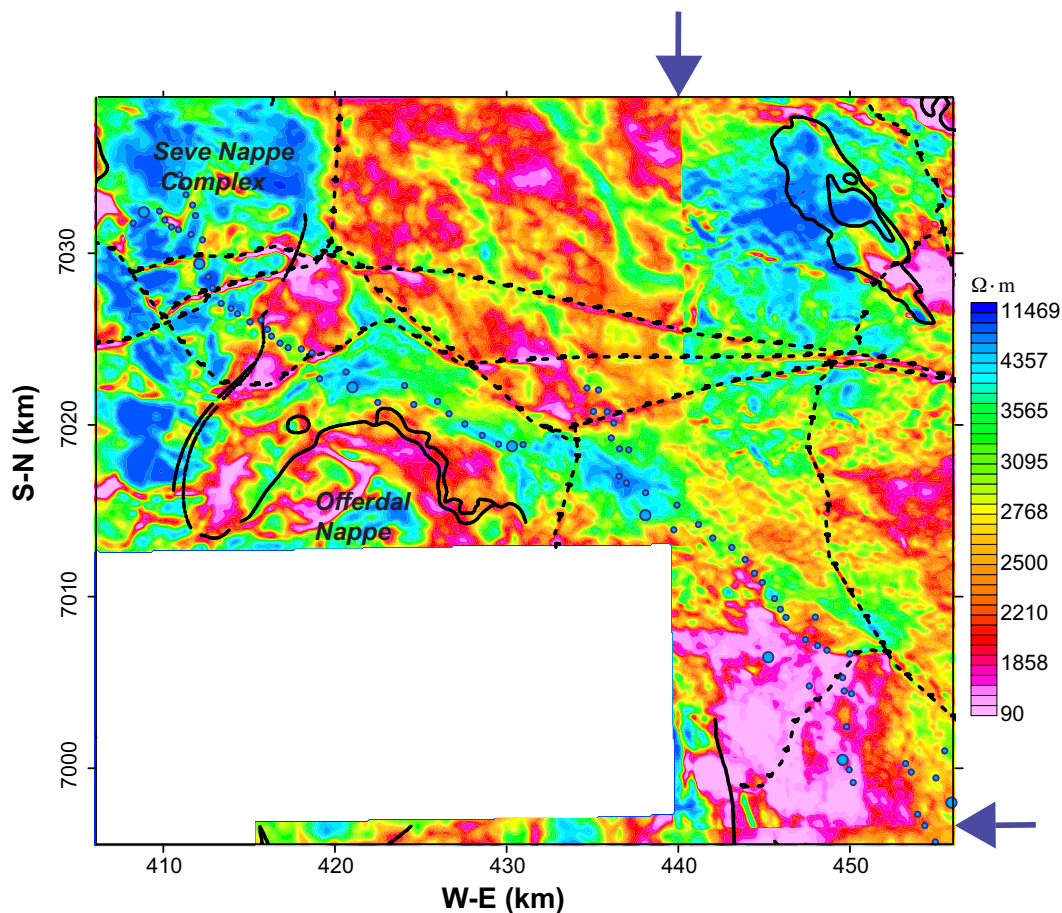
Figure 3. Map of airborne VLF apparent resistivity for the measurement area (courtesy of SGU). The black solid lines show the boundaries between different units from Fig. 2. The black dashed lines are power lines, which cause the linear features in the VLF map. Locations of our broad-band MT stations are marked by small and big blue dots (*cf.* Fig. 2). Note, that the apparent resistivities are discontinuous across the lines W–E = 440 km and S–N = 6996.5 km (marked by arrows), because the map was compiled from three datasets which were collected in different years.

Labson 1991; Sharma *et al.* 2014). In the VLF map, the linear features are caused by power lines (indicated by dashed black lines in Fig. 3). There are two areas where the apparent resistivities are very high, one located in the northwest and the other located in the northeast. Compared to the geological map in Fig. 2, the northwestern high-resistivity anomalies (>4000 $\Omega \cdot$ m) are caused by the Seve Nappe Complex and have a very clear boundary to the units of the Lower Allochthon in the east with apparent resistivities of ∼100–2000 $\Omega \cdot$ m. The northeastern high-resistivity anomalies (>3000 $\Omega \cdot$ m) seem to be related to the Silurian formations (light blue colour in Fig. 2). In the central parts of the study area near Lake Liten, to the south of the MT stations, Silurian turbidites are also present with high apparent resistivities (∼3000–4500 $\Omega \cdot$ m), suggesting that Silurian turbidites are more resistive than Ordovician turbidites but not as resistive as the Seve Nappe Complex. The half-circle-shaped boundary between the Offerdal Nappe and the Baltoscandian sedimentary cover in the geological map in Fig. 2 (brown to blue transition) can also be recognized in the VLF map. The medium resistivities in the central part, to the north of the MT stations, have a shape similar to that of Lake Liten, and two linear anomalies with medium resistivities in the north seem to follow two small rivers. The low resistivity anomaly (∼90–1000 $\Omega \cdot$ m) in the southeastern corner suggests that there might be some conductive rocks in the near surface in this area which are not distinguished in the geological map.

To guide the COSC drilling project, further geophysical surveys were conducted in western Jämtland in the last few years. In preparation for the drilling, a high-resolution 2-D reflection seismic profile was acquired in the Åre-Mörsil area in 2010 (Hedin *et al.* 2012; Fig. 2), followed up by a subsequent reflection seismic survey in the Mörsil-Hallen area in 2014 (Juhlin *et al.* 2016; Fig. 2). The complete reflection seismic image, together with two possible geological interpretations (Hedin *et al.* 2012; Juhlin *et al.* 2016) is shown in Fig. 4. In Hedin *et al.* (2012), a fairly continuous reflection in the section, at a depth between 4.5 km in the west and 2.5 km at CDP (common depth point) 3000 in the central part of the profile, was interpreted as the main décollement surface separating the Precambrian basement from the Caledonian allochthons (Fig. 4a). Owing to the results of our MT survey, which prove the conductive alum shales of the Lower Allochthon to be located at much shallower depth than previously thought, Juhlin *et al.* (2016) re-interpreted the CSP and suggested a correspondingly shallow detachment horizon only a few hundred metres below the top of the alum shales and still inside the conductive layer. In this favoured interpretation, the detachment horizon is located at depths of 3.5 km underneath COSC-1 in the west, 1.2 km at CDP 3000 in the central part of the profile and 600 m in the east. It coincides with a laterally continuous seismic reflection and the reflectivity pattern of the immediately overlying units indicates imbricated structures. The location of the first borehole, COSC-1, targeting the Seve Nappe Complex was
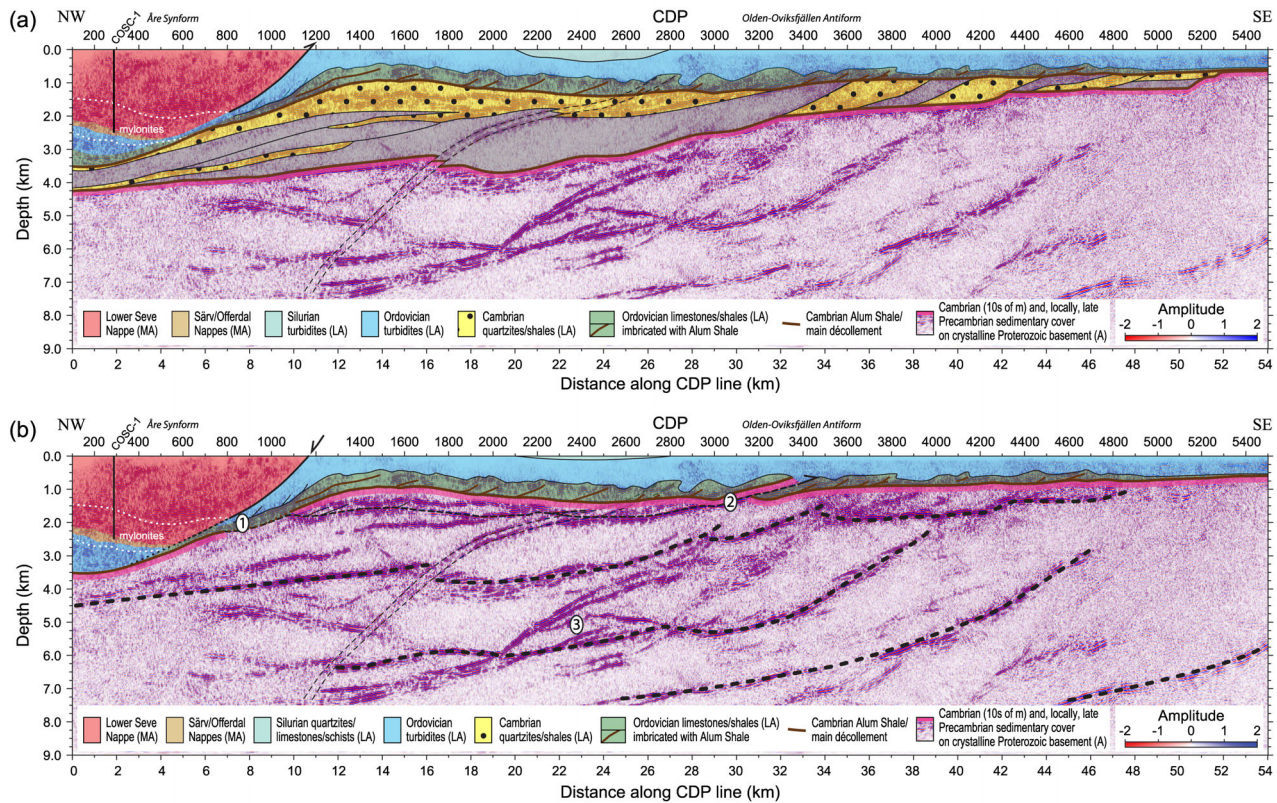
Figure 4. Reflection seismic image (Juhlin *et al*. 2016) overlain with (a) the original geological interpretation from Hedin *et al*. (2012) based on the CSP image with a deep main décollement and (b) the new and preferred geological interpretation from Juhlin *et al*. (2016) based on our MT data and a re-interpretation of the CSP image showing a shallow main décollement.

proposed mainly based on the seismic results. A 3-D interpretation of the Seve Nappe Complex presented by Hedin *et al.* (2014) was based on surface geology, available seismic sections and 3-D inverse modelling of more than 300 ground gravity measurements from SGU. A maximum depth extent of 2.5 km of the Seve Nappe Complex was supported by the inversion models, an interpretation generally consistent with the reflection seismic image. New high-resolution aeromagnetic data, consisting of 130 acquisition lines with a line and point spacing of 200 and 7 m, respectively, were acquired by SGU in 2011. These were modelled and interpreted by Hedin *et al.* (2014) and used by Juhlin *et al.* (2016) to constrain the interpretation of the complete seismic profile. Furthermore, 3-D seismic data were acquired in 2014 around the COSC-1 borehole, which provide more precise information on the 3-D geometry of the structures around it (Hedin *et al.* 2016).

2 BOREHOLE LOGGING

The first borehole (COSC-1, Fig. 2) was drilled near the town of Åre in Jämtland in May to August 2014 using bit diameters of 96 mm from the surface to 1616 m depth and 75 mm from 1616 m depth to the bottom of the hole at *ca*. 2500 m depth. To a depth of 500 m, the drilling fluid was fresh water. At greater depth, a biodegradable polymer was added to the drilling fluid in order to reduce friction. The effect of the drilling mud on the resistivity logs presented below is negligible, because the borehole was flushed with fresh water after drilling was completed (i.e. before the resistivity logs were recorded). To stabilize the uppermost part of the borehole, steel casing was installed down to 103 m depth below ground surface. The borehole is nearly vertical with a small horizontal deviation

of 100 m over its entire length. Since the borehole was drilled into metamorphic rocks, we assume the invasion zone to be only weakly developed.

Two types of borehole resistivity logs were acquired in COSC-1: (1) short and long normal resistivity logging, including self-potential (SP) measurements with a sampling interval of 1 cm in depth conducted by Lund University and (2) shallow and deep laterologs with a sampling interval of 10 cm conducted by the Operational Support Group (OSG) of the International Continental Scientific Drilling Program (ICDP). Both borehole systems were lowered into the well using a wireline.

2.1 Geology of retrieved core in COSC-1

COSC-1 sampled a thick portion (∼2350 m) of the Lower Seve Nappe and possibly ∼150 m of underlying lithologies (Fig. 5). The lower ∼800 m were drilled in a thrust zone where mylonite occurs with increasing frequency and thickness with depth. These mylonite-dominated rocks indicate strong but broadly distributed strain at these depths (Lorenz *et al.* 2015a,b; Juhlin *et al.* 2016). Although the drill hole did not penetrate the bottom of the main thrust zone as planned, lower-grade metasedimentary rocks were encountered intercalated with thick mylonites in the lowermost part of the drill hole (from ∼2350 to 2500 m, Fig. 5; Lorenz *et al.* 2015a,b). Their tectonostratigraphic position is still unclear, but it is likely that they were derived from the Särv or Offerdal Nappe. The second borehole (COSC-2, in the planning phase) will be located further to the east and is planned to penetrate through the Ordovician turbidites, the underlying units of the Lower Allochthon, the main décollement and associated parautochthonous Cambro-Ordovician
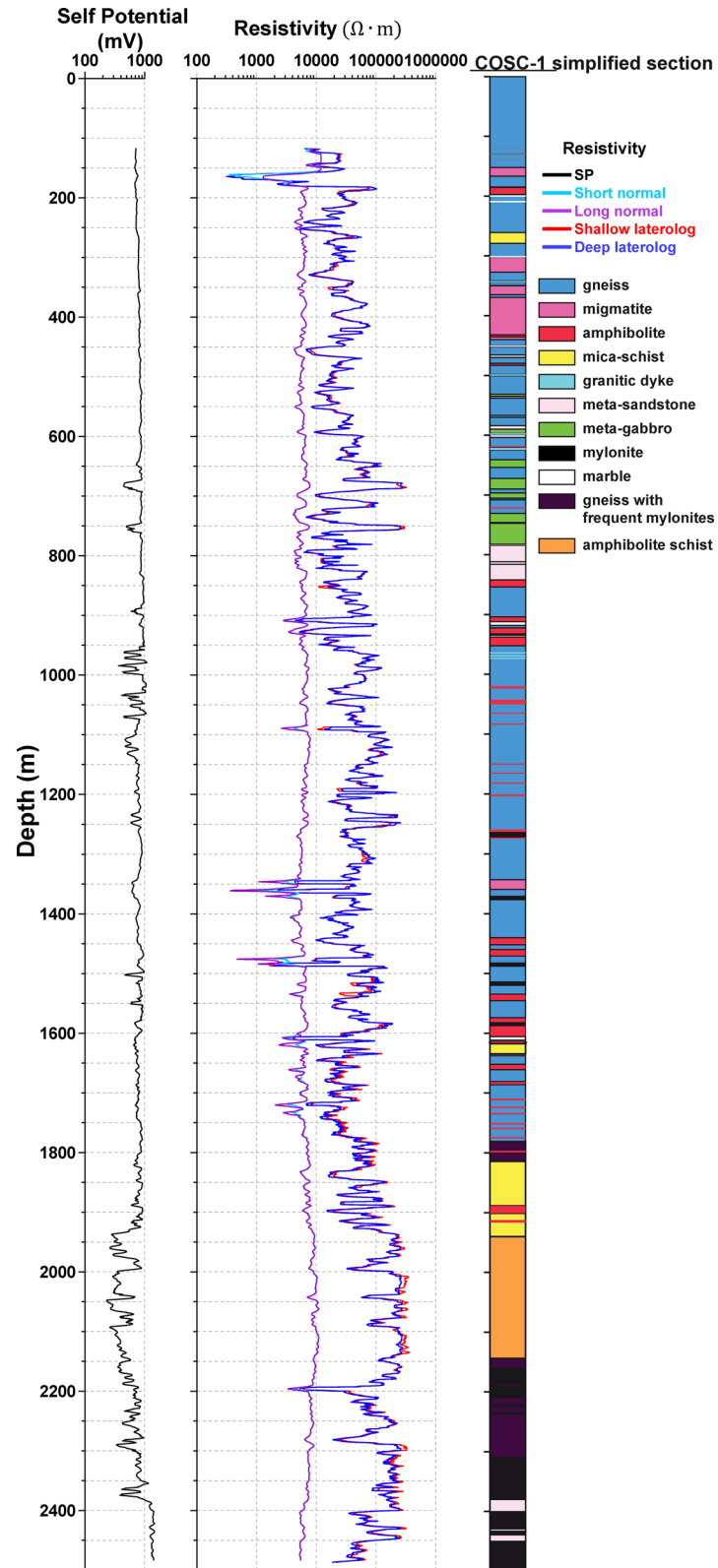
Figure 5. Logs of borehole COSC-1: self-potential (SP, black curve), short and long normal resistivity logs (light blue and purple curves, respectively; the short-normal log is covered by the long-normal log) and shallow and deep laterolog (red and blue curves, respectively) compared to rock units identified from the retrieved core (Lorenz *et al.* 2015a,b). The boundary between the Lower Seve Nappe and underlying nappes was interpreted to occur at 2350 m depth. Rocks were mylonitized from *ca.* 1700 m depth to the bottom with extent increasing with depth.

2.2 Electrical logging methods

In the following descriptions of normal resistivity logs and dual-laterologs, we assume for simplicity that the borehole is vertical.

In normal resistivity logging (Robinson & Çoruh 1988; Ellis & Singer 2007), a potential electrode N is located on the surface, the cable armour above an insulated piece of cable (bridle), which attaches the cable armour to the probe, is used as a sink electrode B, and a source electrode A and a second potential electrode M are placed on the borehole probe. Typical probe lengths are 2.5–3 m. Electrode B is far away from electrode A, about 15 m. The AM spacing is 16 inches (0.41 m) for short normal resistivity logging and 64 inches (1.63 m) for long normal resistivity logging. The horizontal investigation depths perpendicularly away from the borehole are ~0.5–1 and ~1.5–2.5 m for the short normal and long normal resistivity logs, respectively (Ulugergerli 2011), which makes long normal logging less affected by the borehole and any potential invasion zone than short normal logging (Anderson 2001; Ellis & Singer 2007). The current rays for normal resistivity logging are radial in conductive borehole mud and change to vertical or almost vertical in a homogeneous host formation, indicating that normal resistivity logs mostly reflect vertical changes of the resistivity (Ellis & Singer 2007). However, bedding may lead to more radial current flow. Since the AM spacing is much smaller than the other electrode separations, the measured resistivity represents an average resistivity between electrodes A and M. In highly resistive formations with resistivities in excess of ~10 000 $\Omega \cdot$ m, normal resistivity logs exhibit significant bias towards lower resistivities.

In the dual-laterologging method (Robinson & Çoruh 1988; Ellis & Singer 2007), the sink electrode B is located at the surface, the reference potential electrode N is located down the well, whereas the source electrode A and the potential electrode M are both placed on the probe. Using additional guard (or focusing) electrodes on the probe, the currents can be forced to focus on the vicinity of the well (shallow laterolog) or to flow radially outwards from the well (deep laterolog). Thus, the shallow laterolog configuration is sensitive to both vertical and horizontal variations in resistivity, whereas the deep laterolog configuration is predominantly sensitive to horizontal variations in resistivity. The dual-laterolog system used by OSG is of type laterolog-3 (LL3), that is it operates three current electrodes at depth—the source electrode A and two guard electrodes—emitting a low-frequency rectangular current at a base frequency of 115 Hz. To switch between shallow and deep laterolog measurements, short or long guard electrodes are used. The total length of the probe is 3.5 m. The penetration depth of the currents systems is roughly three times the length of the guard electrodes (Telford et al. 1990), suggesting penetration depths of ~0.4 and ~2.4 m for the shallow and deep laterolog modes of the instrument operated by OSG. Following Robinson & Çoruh (1988), the invaded zone may have a proportionally larger effect on the laterolog than the normal resistivity logs. However, in highly resistive formations, dual-laterolog systems do not exhibit systematic downward bias of apparent resistivities at a level comparable to that of the normal log.

It is important to note that the normal and laterolog resistivities are not the true resistivities of the Earth, but apparent resistivities representing volume averages. Nevertheless, the reasoning above suggests that deep laterolog resistivities may be appropriate for usage as reference resistivities in inversion of MT data given appropriate averaging (see below).

SP surveys measure the naturally occurring potential difference between an electrode mounted on the sonde and another electrode placed on the surface. SP logs provide an accurate means of locating bed boundaries because of the associated sharp changes in the SP anomaly (Robinson & Çoruh 1988).

2.3 Electrical log data and comparison to lithological log of COSC-1

The lithology and the resistivity logging data are shown in Fig. 5. The similarity between the short and long normal resistivity logs may suggest that the invasion zone is only weakly developed. Both the normal and laterolog resistivities are quite high. The laterolog resistivities (5000–300 000 $\Omega \cdot$ m) are about one order of magnitude higher than the normal resistivities (200–12 000 $\Omega \cdot$ m) but the shapes of the variations look similar over most intervals. The discrepancies are due to the different electrode layouts of the instruments that cause different current systems and depths of penetration. As noted above, normal resistivity logs underestimate the resistivities of highly resistive formations in a systematic way (this is very likely an effect of the current flowing through the well rather than the formation). Therefore, the comparison of the normal and laterolog resistivities suggests that only the laterolog resistivities should be used for quantitative interpretation. Furthermore, the laterolog resistivities are often as high as 300 000 $\Omega \cdot$ m at depths of 1900 m and more. Since these resistivities are outside the range specified for the instrument, they should not be employed for quantitative interpretation either. Generally, the SP increases when the normal resistivity decreases and vice versa.

Compared with the lithology, the following observations can be made:

(1) The resistivity curves (in particular the laterologs) vary strongly, even within the same rock types, indicating that heterogeneity of the rock units may affect the resistivity logs.

(2) Units of meta-gabbro cause high resistivity anomalies and strong variations in the SP curve at depths between 600 and 800 m.

(3) Between 1800 and 2300 m depth, where the Lower Seve Nappe is mylonitized to an increasing extent (with depth) and the strain is strong and broadly distributed, the logging resistivities are high whereas the SP curve oscillates significantly at comparatively low values of 300 mV.

(4) Below 2300 m depth, near the lower boundary of the Lower Seve Nappe, that is where metasandstones begin to appear occasionally (Lorenz et al. 2015a,b), the logging resistivities decrease whereas the SP increases.

2.4 Use of resistivity logs as prior information in MT inversion

The resistivity logging data can be used as constraints in inversion of the MT data. For this purpose, as normal resistivity logging data and laterologs are typically collected every centimetre or decimetre, the resistivities have to be averaged vertically to match the resolving power of the MT data, which is sensitive to larger volumes of rock. Following Pedersen et al. (1992), the average resistivity for horizontally and vertically flowing currents over the depth interval $(z - \Delta z, \ z + \Delta z)$ are denoted as $\bar{\rho}_{hor}$ and $\bar{\rho}_{ver}$ and are defined as:

$$\frac{1}{\bar{\rho}_{hor}(z)} = \frac{1}{2\Delta z} \int_{z-\Delta z}^{z+\Delta z} \frac{1}{\rho(\xi)} d\xi \tag{1}$$

and

$$\bar{\rho}_{ver}\,(z) = \frac{1}{2\Delta z} \int_{z-\Delta z}^{z+\Delta z} \rho\,(\xi)\,\mathrm{d}\xi, \tag{2}$$

where $\rho(\xi)$ is the measured resistivity from resistivity logging. Considering the acquisition geometries of the resistivity logs, eqs (1) and (2) can be used for vertical averaging of deep laterologs and long normal resistivity logs, respectively. This averaged prior information from borehole logs is to be imposed only on those cells of a 2-D model that are intersected by boreholes. To avoid poor data fit caused by a partly overdetermined inverse problem, the widths (and heights) of 2-D model cells have to be sufficiently small (Ory & Pratt 1995), that is smaller than the local MT skin depth typically leading to cell widths in the range of tens to a few hundred meters in the central parts of 2-D models for higher-frequency MT data. Hence, we impose prior information from borehole resistivity logs directly only over such distances, that is over one horizontal cell width and one vertical cell height. However, the prior information will be spread horizontally and vertically away from cells intersected by boreholes through the smoothness constraints employed as model regularization. How far this information may spread in the model depends on the strength of the regularization and on the distance from a borehole, to which MT data from stations off the borehole are consistent with the prior constraints. Please, refer to Appendix A for further reasoning and details on how resistivity logs can be implemented as prior constraints in the 2-D inversion of MT data.

3 OVERVIEW OF MT THEORY

MT is a passive EM geophysical method which measures natural geoelectric (E) and geomagnetic (H) field variations simultaneously at the surface in the period range of 0.1 ms to 100 000 s to image the electrical resistivity distribution at depth (Berdichevsky & Dmitriev 2008; Chave & Jones 2012). The basis of MT was founded by Cagniard (1953) and Tikhonov (1950). Since then, great improvements have been made in theory, instrumentation, processing, modelling, inversion and interpretation, establishing MT as a suitable geophysical method for a broad range of geological targets. Here, we introduce some basic MT principles which are required to understand the rest of the paper.

In the field, time series of five field components E_x, E_y, H_x, H_y, H_z are collected (x and y indicating perpendicular horizontal directions, with x pointing towards magnetic north, y pointing towards magnetic east and z indicating vertical direction). At MT periods, the field components obey the following relations at the Earth's surface in the frequency domain (Berdichevsky & Dmitriev 2008):

$$\begin{bmatrix} E_x \\ E_y \end{bmatrix} = \boldsymbol{Z} \begin{bmatrix} H_x \\ H_y \end{bmatrix} = \begin{bmatrix} Z_{xx} & Z_{xy} \\ Z_{yx} & Z_{yy} \end{bmatrix} \begin{bmatrix} H_x \\ H_y \end{bmatrix} \tag{3}$$

and

$$H_z = \boldsymbol{T}^{\mathrm{T}} \begin{bmatrix} H_x \\ H_y \end{bmatrix} = \begin{bmatrix} T_x \\ T_y \end{bmatrix}^{\mathrm{T}} \begin{bmatrix} H_x \\ H_y \end{bmatrix}, \tag{4}$$

where $\boldsymbol{Z}$ is the impedance tensor relating horizontal electric and magnetic fields and $\boldsymbol{T}$ is the tensor of vertical magnetic transfer functions (VMTF) of a medium. Note, that the components of the electric and magnetic fields and, thus, the tensors are frequency

dependent quantities. The components of the impedance tensor are commonly represented as apparent resistivity ρ_a and phase φ:

$$\rho_{a,ij} = \frac{1}{\omega\mu_o}\,\big|Z_{ij}\big|^2, \quad \varphi_{ij} = \mathrm{atan}\left(\frac{\mathrm{Im}\,Z_{ij}}{\mathrm{Re}\,Z_{ij}}\right), \tag{5}$$

where ω is angular frequency, μ_0 is the magnetic permeability of free air, and the subscript ij indicates an arbitrary combination of x and y. A preliminary guess of the effective depth can be calculated from field observations using Schmucker's (1987) z^* method:

$$z^* = \sqrt{\rho/(\omega\mu_0)}\,\sin\varphi. \tag{6}$$

Under 2-D conditions with x being the geoelectrical strike direction, the impedance tensor $\boldsymbol{Z}$ and VMTF $\boldsymbol{T}$ satisfy

$$\boldsymbol{Z} = \begin{bmatrix} 0 & Z_{xy} \\ Z_{yx} & 0 \end{bmatrix} = \begin{bmatrix} 0 & Z_{\mathrm{TE}} \\ Z_{\mathrm{TM}} & 0 \end{bmatrix}, \tag{7}$$

$$\boldsymbol{T} = \begin{bmatrix} 0 & T_{\mathrm{TE}} \end{bmatrix}, \tag{8}$$

respectively, and inversion models may be obtained by combining up to three different transfer functions: Z_{TE} (the impedance of the transverse electric (TE) mode, also called E-polarization, with telluric current flowing along strike and thus sensitive to conductors), Z_{TM} (the impedance of the transverse magnetic (TM) mode also called B-polarization, with telluric current crossing structures and thus sensitive to resistors) and T_{TE}. However, if a preferred strike direction cannot be found (in a 3-D case), inversions of approximate 2-D transfer functions Z_{TE}, Z_{TM} and T_{TE} for 2-D models will be misleading. To minimize the effect caused by this problem, Pedersen & Engels (2005) proposed to invert the determinant impedance $Z_{\mathrm{DET}} = \sqrt{Z_{xx}Z_{yy} - Z_{xy}Z_{yx}}$, which is rotationally invariant and less prone to introducing artefacts from 3-D effects into 2-D models.

A small-scale 2-D or 3-D near surface inhomogeneity with dimensions much smaller than the MT skin depths of the host rock and the inhomogeneity will cause galvanic distortion in measurements at adjacent MT stations. The distorted impedance tensor $\boldsymbol{Z}$ and the undistorted impedance tensor $\boldsymbol{Z}_0$ have the following relationship (Wannamaker *et al.* 1984; Kalscheuer *et al.* 2012, 2015):

$$\boldsymbol{Z} = (\mathbf{I} + \boldsymbol{P}_h)\,\boldsymbol{Z}_0(\mathbf{I} + \boldsymbol{Q}_h\boldsymbol{Z}_0)^{-1}, \tag{9}$$

where $\mathbf{I}$ is the identity matrix and $\boldsymbol{P}_h$ and $\boldsymbol{Q}_h$ are the distortion tensors of the horizontal electric field and horizontal magnetic field, respectively.

4 MT DATA ACQUISITION, PROCESSING AND ANALYSIS

In 2013, 83 broad-band MT stations were deployed along the CSP (Fig. 2) using a station spacing between 500 and 1000 m. In the far western part of the measurement area, stations were positioned along two shorter branches in the vicinity of COSC-1 (Fig. 2). Note, that we selected the stations from the southern branch for the following processing and inversion steps, meaning that 5 stations from the northern branch were neglected and that the data of 78 broad-band stations were subject for further analysis. Five instruments were used: two from Uppsala University with three magnetic sensors, and three from ITSAK, Greece, with only two sensors for the horizontal magnetic field components. Thus, while time series for the four horizontal electric and magnetic fields (E_x, E_y, H_x, H_y) were recorded at all the stations, those for the vertical magnetic field (H_z) were recorded only at about one third of them. All instruments used

non-polarizable electrodes (Uppsala University) and MFS06 induction coils (Metronix). Three different sampling rates were applied: 20 Hz for about 21.5 hr, 1000 Hz for 2 hr starting from midnight and 3000 Hz for about half an hour during daytime.

The MT transfer functions Z and T were calculated using Smirnov's (2003) algorithm MTU2000, which applies amongst other processing, levelling and notch filtering (removing power line signals) to the segmented time series, uses a robust estimation procedure with a high break-down point and has an option for remote reference processing (Gamble *et al*. 1979). MT data from sites in northern Sweden and northern Norway (Cherevatova *et al*. 2015) recorded at the same time as our data were used for remote referencing. In addition, stations recorded simultaneously in our measurement area were also used as remote references, although the distance between the processing station and the remote reference station would be only 500–3000 m in most cases. Whenever the impedance tensors or VMTFs showed improvement, the results of remote reference processing were preferred over single site processing. For each station, the obtained impedance tensors and VMTFs from the three different sampling rates were merged into one, yielding a total period range of 0.0014–1000 s. For many stations, the day recordings of 3000 Hz were too noisy and had to be deleted, which set the minimum signal period to 0.0033 s.

Fig. 6 shows the apparent resistivities and phases of the off-diagonal components Z_{xy} and Z_{yx}, the diagonal components Z_{xx} and Z_{yy} and the determinant impedance Z_{DET} with x and y oriented in a rotated coordinate system for 8 sites, the locations of which are marked as the larger dots with light blue filling and dark blue outline in Figs 2 and 3. The following patterns can be clearly observed: the apparent resistivities of the stations in the west (small site numbers; ∼10 000 Ω · m at the shortest periods) are higher than those of the stations in the east (big site numbers; ∼100 Ω · m at the shortest periods); the apparent resistivities decrease rapidly over the period range of 0.002 to 1 s and decrease slowly (are almost constant) thereafter; the phases are about 60° at the shortest period; at the most western sites phases oscillate between high and low values, while in the central and eastern parts of the profile phases rise to almost 90° at ∼0.01 s to decay again between 0.1 and 1 s.

Data quality varies from very good mostly at the eastern end of the profile, to noisy nearby urban areas. The main sources of noise are infrastructure and power lines in the study area (see Fig. 3); noise of the latter source was mostly removed by the notch filters of the processing software. Given the great variation of data quality, all transfer functions were systematically checked through 1-D inversions (e.g. Smirnov & Pedersen 2009). The results of these inversions highlighted potentially problematic sites (49 of 78) that were visually inspected and edited prior to dimensionality and strike analysis and inverse modelling. More than half of the inspected sites (30) were found to be disturbed by near-field effects from unknown sources or 3-D effects at longer periods. Of these 30 sites, 24 sites had phases that dropped to zero at ∼1 s and apparent resistivities that increased strongly with increasing period (indicative of near-field effects). To eliminate adverse effects on the strike analyses and inversion models, phases and apparent resistivities of these sites were cut at 0.1 s. Another 6 of these 30 sites had phases out of quadrant (>90°; not possible to reproduce with isotropic 2-D models) and those phases with their corresponding apparent resistivities were removed (for example sites A27 and A36 in Fig. 6). Nineteen sites had to be completely rejected. The remaining data set consists of 59 sites, 25 of which have transfer functions up to 0.1 s instead of 1000 s, reducing significantly the penetration depth along the profile.

The induction arrows (computed from the VMTFs) for six selected periods (0.0078, 0.088, 1, 11.314, 128 and 724.08 s) are shown in Fig. 7, using the Wiese convention (Wiese 1962), in which the real induction arrows point away from conductors. The lengths of many induction arrows are larger than 0.5, suggesting that the VMTFs are strongly contaminated by noise. Therefore, the VMTFs were not considered for subsequent inversions.

Before inversion, strike and dimensionality analyses were conducted to determine to what extent the 3-D resistivity distribution can be approximated in 2-D. For the western part of the investigation area, the aeromagnetic map and the regional gravity map (Hedin *et al*. 2014) and the seismic data (Juhlin *et al*. 2016) suggest that the structure is 3-D. In contrast, in the central and eastern parts, the reflection seismic data support the idea that the structure at depth can be approximated as 2-D. Korja *et al*. (2008) found a predominant geological strike direction of N40°E for the eastern part of their MT profile recorded between the Norwegian border and the Caledonian front.

For MT data, Zhang's strike and distortion model (Zhang *et al*. 1987), Bahr's phase-sensitive skew (Bahr 1991) and the phase tensor (Caldwell *et al*. 2004) were used for dimensionality and strike analyses.

Among our selected 59 sites, the western 13 sites have Bahr's skews that are random and most of them are higher than 0.3, while for the remaining sites, almost all the Bahr's skews are lower than 0.3. This suggests that the geoelectrical structure in the central and eastern parts of the profile may be 2-D, but confirmation from other dimensionality analyses is needed. Consistently, the skew angle β (Fig. 7) from the phase tensor method (Caldwell *et al*. 2004) shows high values for most of the western stations and small values for most of the central and eastern stations. Note, that the skew angles at a period of 128 s are comparatively high indicating possible 3-D effects. However, closer inspection of the data and their errors suggests that these high skew values are caused by noise in the data. Moreover, when we computed misfit values $\sqrt{Q}$ using Zhang *et al*.'s distortion model (e.g. Zhang *et al*. 1987; Smirnov & Pedersen 2009; Bastani *et al*. 2011) with fixed strike angles (e.g. Fig. 8d), high values of $\sqrt{Q}$ for the western 13 sites and comparatively low values for the central and eastern sites were obtained no matter what strike angle we chose. This implies a 3-D structure in the western part; while in the central and eastern parts of the profile, the resistivity structure can be approximated as 2-D. Furthermore, for most of the stations in the central and eastern parts of the profile with periods shorter than ∼1 s, the apparent resistivities and phases of Z_{xy}, Z_{yx} and Z_{DET} are very similar, indicating 1-D structure at shallow depth. This is supported by small values of $\sqrt{Q}$ for all assumed strike angles.

The computed strike angles for each station and each period using Zhang's, Bahr's and the phase tensor methods are shown in Figs 8(a)–(c). Rose diagrams of the calculated strike angles for all stations and periods are plotted in light blue, showing no preferred strike directions; while those for the central and eastern stations with periods longer than 1 s are plotted in black, suggesting a regional strike angle of N20°E–N40°E. For periods shorter than 1 s, the computed strike angles are often >50 degrees in the central and western parts of the profile (Figs 8a–c). As discussed before, these shorter-period data carry a strong 1-D signature. Hence, their estimated strike angles are not stable, and these shorter-period data can equally well be explained using a regional strike angle of N20°E–N40°E. To further determine the best geoelectrical strike direction, we computed misfit values $\sqrt{Q}$ of Zhang *et al*.'s distortion model for each station and period with fixed strike angles
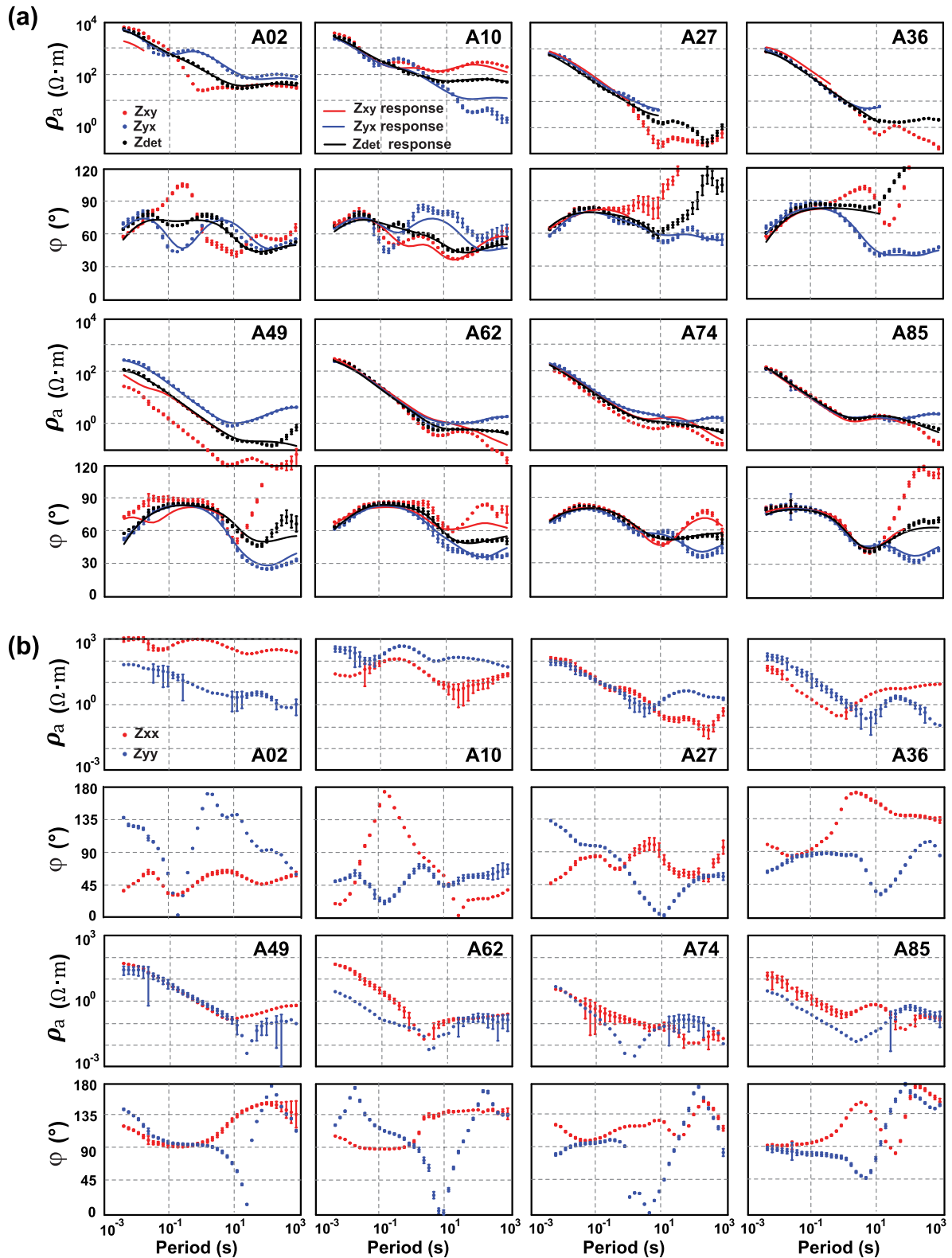
Figure 6. Apparent resistivities ρ_a and phases φ of (a) the $\mathbf{Z_{xy}}$, $\mathbf{Z_{yx}}$ and determinant ($\mathbf{Z_{DET}}$) impedances and (b) the $\mathbf{Z_{xx}}$, $\mathbf{Z_{yy}}$ impedances for eight selected sites, marked in Figs 2, 3, 8 and 9 using big blue dots, station labels or blue triangles. The shown data are in a rotated coordinate system for a presumed strike direction of N30°E (corresponding to 34°E of geographic N after accounting for 4° of magnetic declination). The model responses of the $\mathbf{Z_{xy}}$ (red line; TE mode inversion model in Fig. B1c, Appendix B), $\mathbf{Z_{yx}}$ (blue line; TM mode inversion model in Fig. B1d, Appendix B) and $\mathbf{Z_{DET}}$ (black line; inversion model in Fig. 9) are also plotted in (a).
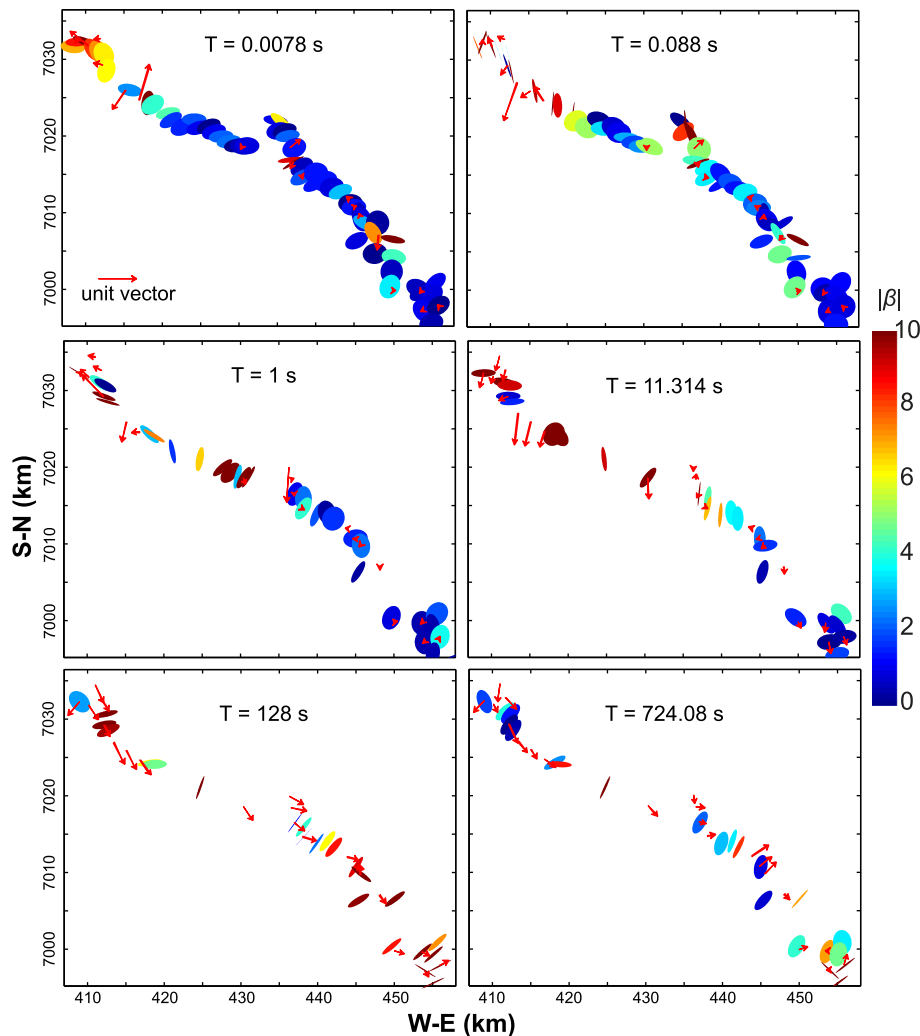
Figure 7. Real induction arrows (red) and the phase tensor ellipses for six selected periods 0.0078, 0.088, 1, 11.314, 128 and 724.08 s in the study area. The phase tensor ellipses are filled with colours which represent the absolute skew angles $|\beta|$ of the phase tensors. Note that owing to the proximity of some stations phase tensor ellipses overlap and some phase tensor ellipses are elongated.

between N10°E and N90°E. As the structure is 3-D in the western part, we only looked at the central and eastern stations in choosing the strike direction. For periods shorter than 1 s, the averaged misfit value $\sqrt{Q}$ is very small and varies only slightly with different fixed strike angles, indicating that the shorter-period data can equally well be explained using any regional strike angle. For periods longer than 1 s, the averaged misfit value $\sqrt{Q}$ varies rapidly and has the smallest values at N30°E with regard to geomagnetic north. Therefore, N30°E was chosen as the regional strike direction (the corresponding misfit values $\sqrt{Q}$ of each station and period are shown in Fig. 8d). Note that the misfit values of the shorter-period data are in fact much smaller than those of the longer-period data. Since the *x*-direction was oriented along magnetic north during the field measurements, the regional strike direction is N34°E with regard to geographic north (accounting for ∼4°E magnetic declination in the measurement area). Since the strike direction is mostly determined by the longer-period data, the difference of 6° with regard to the strike direction of N40°E found by Korja *et al.* (2008) for the MT data recorded along the CCT reflection seismic profile may be related to gradual changes in Precambrian bedrock geology.

5 MT INVERSIONS

5.1 2-D inversions

Before 2-D inversion, the edited 59 stations were projected onto a straight line with the direction of N56°W, as the chosen strike angle is N34°E. The impedances of approximate TE and TM modes were computed with regard to the determined strike direction (see examples in Fig. 6), and the determinant impedances were computed from the full impedance tensors.

In a 3-D/2-D distortion model, that is for local 3-D distorting inhomogeneities and a regional 2-D model, the distorted impedance tensor takes a relatively simple form after rotating the coordinate system to have the *x*-axis aligned with the regional strike direction. In this configuration, the diagonal and off-diagonal elements of any column of the distorted impedance tensor are related to the corresponding regional off-diagonal impedance tensor element in strike coordinates by real and frequency independent distortion coefficients (Zhang *et al.* 1987; Groom & Bailey 1989). In subsequent inversion, the diagonal elements of this configuration are disregarded, because they do not contain additional information on the regional structure as compared to the off-diagonal elements. As already
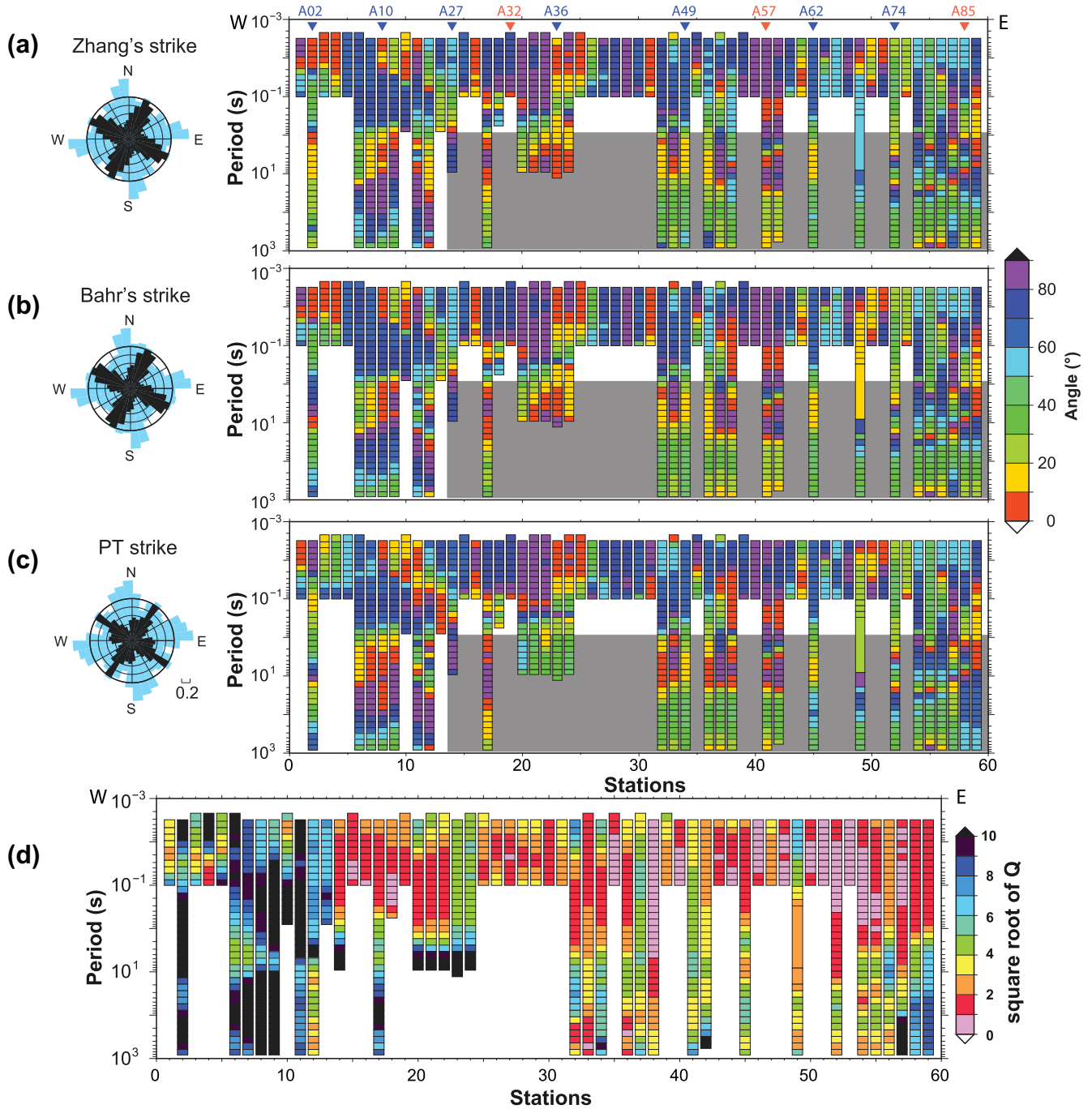
Figure 8. Computed strike angles using (a) Zhang *et al*.'s, (b) Bahr's and (c) the phase tensor approaches and (d) Q-misfit functions resulting from Zhang *et al*.'s (1987) distortion analysis with N30°E as the assumed strike direction (corresponding to 34° E of geographic N). The rose plots in light blue show all the strike results for all the stations and periods, with no preferred strike direction; while those in black show the strike angles for the central and eastern parts of the profile and for periods longer than 0.1 s (marked in grey in the angle distribution plots), with N30°E as the predominant strike direction. Locations of the sites in Fig. 6 are marked in blue and those in Figs 11 and 12 are marked in orange. Results indicate a predominantly 3-D structure in the western part of the profile, whereas the central and eastern parts can be modelled in 1-D for periods shorter than 0.1 s and 2-D for periods longer than 0.1 s.

noted, the off-diagonal elements contain a static shift factor and the corresponding regional impedance tensor elements. Though this is not formally the same static shift factor as in the Groom-Bailey decomposition, in 2-D inversion it can be treated in the same form as the Groom-Bailey static shifts (i.e. by allowing for static shift factors as free parameters in inversion or by down-weighting the apparent resistivities relative to the phases). For the western stations, for example, station A02 in Fig. 6, such a 3-D/2-D distortion behaviour

with the diagonals and off-diagonals from the same column being related by a real and frequency-independent factor is not observable. Once more, this confirms that for the western part of the profile, the data are 3-D and inversions of poor approximations to TE-mode and TM-mode impedances are not really meaningful. In contrast, for stations in the central and eastern parts of the profile such as station A36 in Fig. 6, the 3-D/2-D distortion model is much better fulfilled.
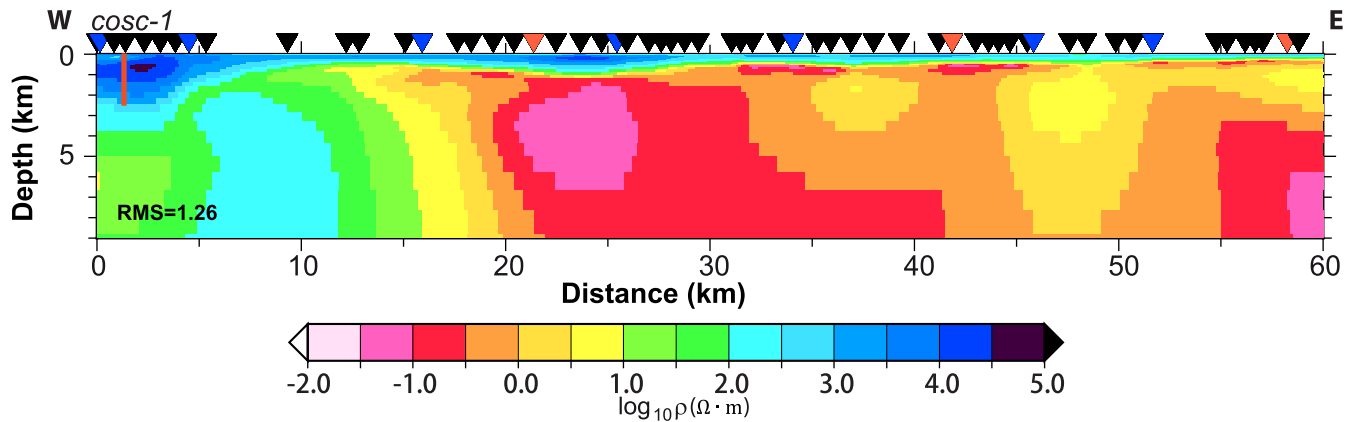
Figure 9. 2-D resistivity inversion model computed from determinant impedances, using a damped Occam scheme and the model resulting from an Occam inversion as the starting model. The location and depth of borehole COSC-1 are marked by a red line. Locations of the sites in Fig. 6 are marked in blue and those in Figs 11 and 12 are marked in orange.

The approximate TE mode (Z_{xy}) and TM mode (Z_{yx}) impedances and the determinant impedances (Z_{DET}) are affected differently by 3-D inductive effects which the strike and distortion analysis cannot account for. Hence, prior to the 2-D inversions, additional data editing to mitigate 3-D inductive effects was performed differently for the different types of impedances. We prefer to invert determinant impedances for 2-D models, because they were shown to be much less influenced by 3-D inductive effects than approximate TE and TM mode impedances (Pedersen & Engels 2005). At several stations, we removed Z_{xy} data with strong 3-D inductive effects above a relatively short period (e.g. above ~0.02 and ~0.3 s for stations A02 and A36, respectively, *cf.* Fig. 6), while the Z_{DET} data and most Z_{yx} data did not require further editing.

We applied the Emilia inversion package, which has two schemes for 2-D MT inversion: an Occam scheme and a damped Occam scheme (Kalscheuer *et al.* 2010; Appendix A). While the former scheme applies general smoothness constraints, the latter one employs additional Marquardt-Levenberg damping for stabilization.

In order to measure how well the data are fitted, the rms misfit is used which has the form

$$rms = \sqrt{\frac{\sum_{i=1}^{n} \left(d_i^{obs} - d_i^{pre}\right)^2 / \sigma_i^2}{n}}, \tag{10}$$

where $\boldsymbol{d}^{obs}$ and $\boldsymbol{d}^{pre}$ are the observed data and model-predicted data, respectively, and σ are the errors of the observed data. To investigate details of the data fit distribution, normalized apparent resistivity ($\frac{\rho_{ai}^{obs} - \rho_{ai}^{pre}}{\sigma_{\rho_{ai}}}$) and phase differences ($\frac{\varphi_i^{obs} - \varphi_i^{pre}}{\sigma_{\varphi_i}}$) for each period and station can be plotted.

Our finite-difference model grid consisted of rectangular cells with 246 horizontal cells (4 cells between 2 abutting stations) and 48 vertical cells. In the vertical direction, the cell thickness increased with a geometric progression using a factor of 1.15 and beginning with a thickness of 10 m at the surface. After an initial trial-and-error procedure, the weights for smoothness in the horizontal and vertical directions were set to 10 and 1, respectively, because this combination gave the lowest rms misfit. This choice of smoothness weights is compatible with the fact that most of the reflections in the seismic section dip more horizontally and, thus, the structures are supposed to have more pronounced resistivity contrasts in the vertical direction. Inversions of four different modes (the determinant, TE, TM and TE + TM impedances) were tested. Here, we focus on

the inversion of determinant impedances using a damped Occam inversion and a starting model that was computed using Occam inversion. For inversion results of TE and TM mode impedances and of determinant impedances using other inversion strategies, please refer to Appendix B.

For the determinant impedances, 10 per cent relative error and 2.85° absolute error were set as the lowest uncertainties for the apparent resistivities and phases, respectively. Both error floors correspond to 5 per cent relative error on impedance. For two sites, where there was evidence for static shift, we used larger errors (90 per cent) for the apparent resistivities. Using a damped Occam inversion with a fixed Lagrange multiplier of 6.3 on the smoothness constraints and a starting model that was computed using Occam inversion, we inverted the determinant impedances resulting in the inversion model shown in Fig. 9 with a total rms = 1.26. In Fig. 10, the corresponding data fits of the determinant impedances are shown as normalized apparent resistivity and phase differences (differences between field and forward data divided by the absolute errors estimated for the field data; *cf.* paragraph containing eq. 10) and the responses for the eight selected stations are plotted as solid black lines in Fig. 6. We can see that the data fits are very good, but with slightly higher misfit values at the lower and higher period ends for some stations.

In general, all the resistivity models inverted from the determinant, TE mode and TM mode impedances exhibit quite similar behaviour (*cf.* Fig. 9 and Appendix B): in the western 10 km of the profile, where the geological unit changes from the Seve Nappe to the Lower Allochthon, a resistor (>1000 Ω · m) is present close to the surface, extending down to 2–3 km depth, below that the structure is more conductive (100–1000 Ω · m); in the central and eastern parts of the profile, a very thin resistive layer (100–10 000 Ω · m) lies at the surface with thickness decreasing from about 1 km in the west to ~300 m in the east, and underneath that layer, the structure becomes very conductive (<10 Ω · m, typically <1 Ω · m). However, the models differ in details. The shapes of the top resistor in the west vary in the different models. This is likely due to the 3-D effects indicated by the quite high misfit values $\sqrt{Q}$ of the strike and distortion analysis in the western part of the profile (Fig. 8). The deeper structures in the central and eastern parts of the profile are different as well.

Based on the differences in rms misfit values, we prefer the models retrieved using inversion of the determinant impedances in
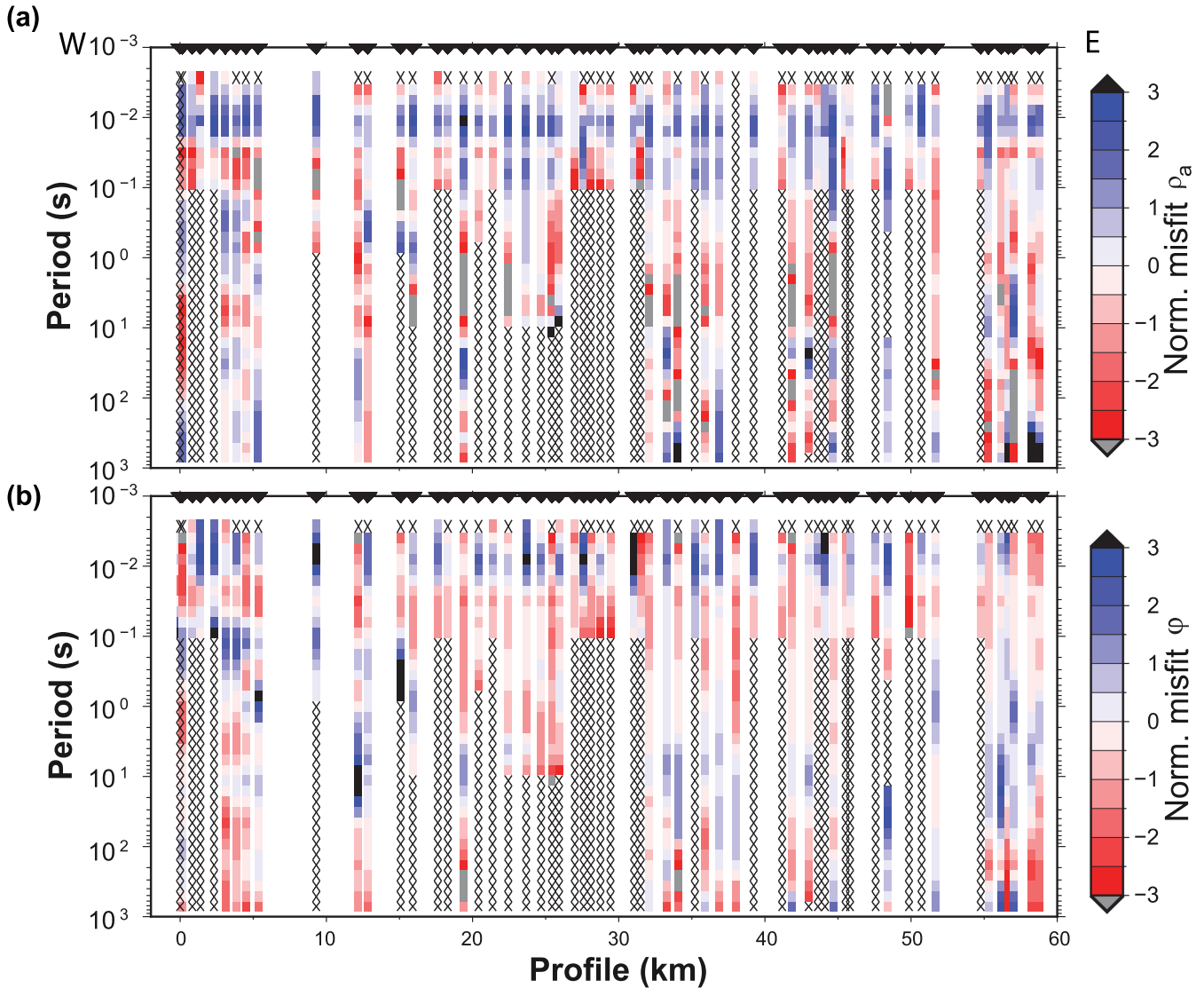
Figure 10. Fits of forward responses of the model in Fig. 9 to (a) the apparent resistivities ρ_a and (b) phases φ of the determinant impedances. Note that the differences between field data and forward responses were normalized by absolute data errors and, hence, are without units. Crosses indicate data that were removed during editing (*cf.* text).

Fig. 9 over those of the TE-mode and TM-mode impedance data in Figs B1(c)–(e) (Appendix B). Furthermore, comparison with the CSP image shows better correlation with the inversion models from the determinant impedances than the TE, TM or TE + TM mode models.

5.2 1-D inversions

For better depth constraints to the highly conductive layer at 300–1000 m depth in the central and eastern parts of the profile, 1-D inversions were conducted for four selected sites within the two areas discussed for COSC-2 by Juhlin *et al.* (2016): A31, A32 and A33 close to CDP 2200 and A57 located 2–3 km SE of CDP 4100. These sites were selected because their diagonal impedance elements are close to zero, and the off-diagonal tensor elements show a high level of similarity. Thus, they satisfy 1-D conditions approximately. With the 1-D inversion algorithm in the Emilia package, the full impedance tensor can be inverted by allowing for electric and magnetic distortion parameters (Kalscheuer *et al.* 2012, 2015).

Layer resistivities, layer thicknesses and galvanic distortion parameters are free parameters in the inversion algorithm, which applies Marquardt-Levenberg damping and minimum-solution-length constraints to layer and distortion parameters, respectively. Note that Marquardt-Levenberg inversion models are better suited to account for sharp resistivity contrasts than smoothness-constrained models. Variation of the starting models with interfaces to the conductor at distinctly smaller or larger depth led to almost identical inversion models, meaning that the depths to the <1 $\Omega \cdot$ m conductor are robust features of the models. Using only two layers, it was possible to satisfy the data constraints almost equally well as using three layers, but led to unreasonably large distortion parameters. Thus, models with three layers were preferred.

The 3-layer 1-D inversion models of sites A32 and A57 (the locations are marked in orange in Fig. 9) are shown in Figs 11(a) and (b). Results for sites A31 and A33 are very similar to those of site A32 and are not shown. As an example, the data fits for site A57 for all four impedance tensor elements are shown in Fig. 11(c). In the 1-D inversion models, conductive layers are encountered at
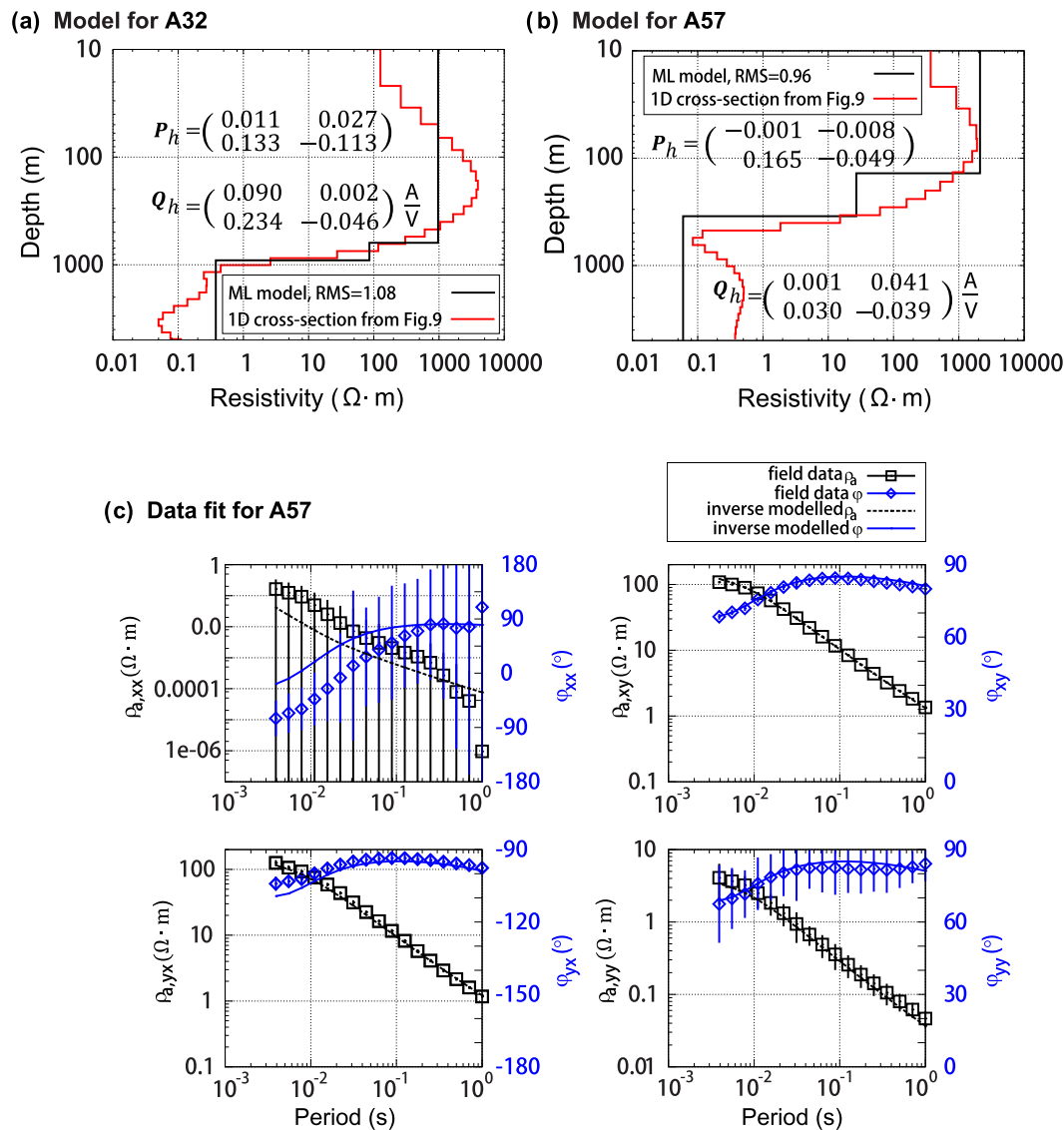
Figure 11. Marquardt-Levenberg (ML) 1D inversion models of stations (a) A32 and (b) A57 in areas discussed for future borehole COSC-2 by Juhlin *et al.* (2016) and (c) fits to the ρ_a and φ of the complete impedance tensor of station A57. The corresponding 1-D cross-sections extracted from the 2-D inversion model in Fig. 9 were also plotted in (a) and (b). $\mathbf{P}_h$ and $\mathbf{Q}_h$ are the matrices consisting of the distortion parameters of the horizontal electric field and horizontal magnetic field, respectively. Layer resistivities, layer thicknesses and galvanic distortion parameters were free parameters in the inversion. A high conductivity layer associated to alum shale is encountered at 900 and 350 m depth underneath stations A32 and A57, respectively. Note that the impedance tensor elements are w.r.t. the original coordinate system in which the data were recorded.

900 and 350 m depth for station A32 and A57, respectively, which correlates well with the 2-D inversion models.

Underneath the eastern end of the profile, well below the shallow conductor at 300–800 m depth, the 2-D model in Fig. 9 suggests the existence of a deep conductive structure (>3 km). We investigated whether such a deep conductive unit is required by the data. For this purpose, we inverted the determinant impedance of station A85 for 4- and 3-layer models accounting for the relevant galvanic distortion parameters. In the resulting 4-layer model (Fig. 12a), a shallow resistive (500 $\Omega \cdot$ m layer down to ~330 m depth, a conductive layer of 0.6 $\Omega \cdot$ m between 330 and 600 m depth, and a relatively resistive layer of 5 $\Omega \cdot$ m down to >3 km depth overlying a conductive basal unit of 0.4 $\Omega \cdot$ m explain the data with a rms misfit of 1.6 (Fig. 12b). In contrast, excluding the basal conductor yields a 3-layer model with an unacceptably high rms of 5.0 (Fig. 12b).

Considering the field data in Fig. 12(b), the resistive unit between the two conductors appears to give rise to a low in phase and weakly pronounced high in apparent resistivity at a period of about 10 s. At stations further west, the data carry an even weaker signature of the intermediate resistive layer (Fig. 6). Hence, we conclude that the data require a deep conductor at the eastern end of the profile. However, its depth and resistivity are not very well determined.

5.3 2-D inversions with borehole logs as prior constraints

We developed additional modules for borehole logs as prior constraints in the Emilia inversion package (Appendix A). Several models were tested to prove the functionality of the proposed constrained inversion algorithm. The tests showed that the algorithm works well
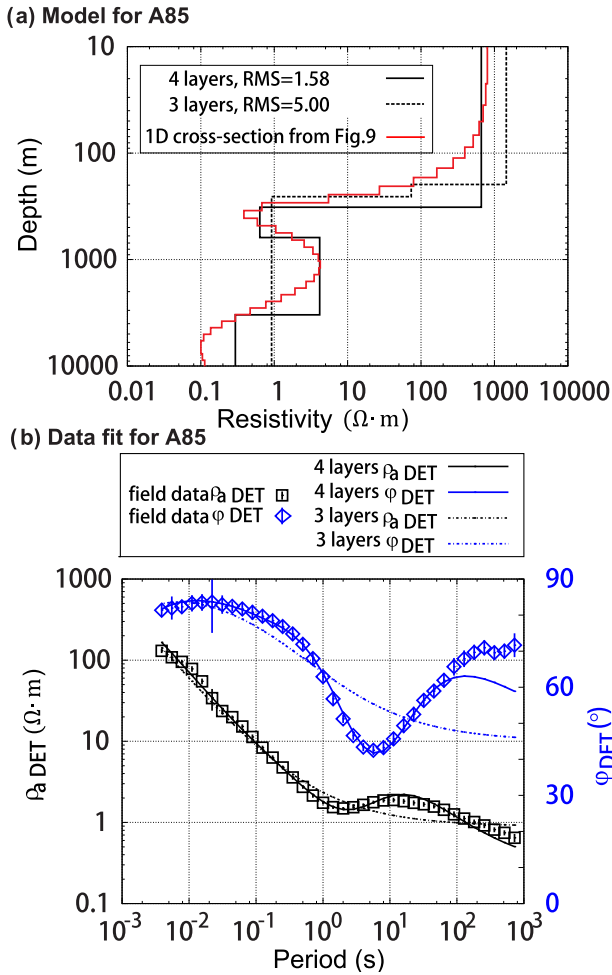
(a) Model for A85

(b) Data fit for A85

Figure 12. (a) Marquardt-Levenberg 1-D inversion models of station A85 using three and four layers and (b) fit of the model responses to the apparent resistivity ρ_a and phase φ of the determinant impedance. The corresponding 1-D cross-section extracted from the 2-D inversion model in Fig. 9 was also plotted in a). Layer resistivities, layer thicknesses and galvanic distortion parameters were free parameters in the inversion. For the 4-layer model, the retrieved distortion parameters are $\mathbf{C} = \det(\mathbf{I} + \mathbf{P_h}) = 0.80$, $\mathbf{D} = \det(\mathbf{Q_h}) = -0.2(A/V)^2$ and $\mathbf{G} = \mathbf{Q_{yx}} - \mathbf{Q_{xy}} = 0.08A/V$ (*cf.* Kalscheuer *et al.* 2012). Conductive alum shale is encountered at 400–600 m depth and the >3000 m deep conductor may represent a unit of graphite schist. Clearly, the 3-layer model without the deep conductor fails to explain the data.

when we use the true resistivities of the subsurface layers as borehole log constraints. The borehole can be of any shape and the number of boreholes is not limited.

As indicated by our above discussion of the long normal and the deep laterolog resistivities, we present only the inversion model that employed the deep laterolog resistivities from COSC-1 as prior constraints. To compute prior resistivities, the deep laterolog resistivities in the depth range of 110–1900 m (i.e. between the lower end of the borehole casing and the depth range with unreliable laterolog resistivities of ~300 000 $\Omega \cdot$ m) were averaged over the thickness of the corresponding 2-D model cells intersected by the borehole using eq. (1), and the standard deviations from these averaged logging resistivities within each cell were used as reciprocal weights (matrix $\mathbf{W}_{bh}$ in eq. A1). Note that all 2-D model cells coinciding with COSC-1 are 140 m wide. The model resulting from inversion of the determinant impedance data using borehole constraints is shown in Fig. 13(a) and was computed using a damped Occam

approach using a fixed Lagrange multiplier of 6.3 on the smoothness constraints. Compared with the model in Fig. 9, the borehole constraints introduced changes only to the resistor in the western part of the profile around the borehole. The inversion model presented in Fig. 13(a) exhibits smooth variations of resistivity around COSC-1, indicating the consistency of the borehole log and the MT data. As evident in Fig. 13(b), the largest observed changes in resistivity relative to the 2-D model in Fig. 9 correspond to a factor of 2, and the averaged deep laterolog resistivities are reproduced by the constrained inversion within the assigned uncertainties. In the following section, the geological interpretation is based on the resistivity model in Fig. 13(a) which is obtained from the inversion for the determinant impedance with the averaged deep laterolog resistivities as prior constraints. The part of the inversion model outside the enlarged area in Fig. 13(a) is virtually identical to the model in Fig. 9 that was computed without borehole constraints. Similar to the model structures, the data fit of the sites adjacent to the borehole did not change much (the differences in rms per station are less than 0.008 at sites adjacent to COSC-1). Hence, similar to identical conclusions can be drawn from the inversion model without constraints in Fig. 9.

Next, we present a synthetic test to evaluate how constraints from a future borehole (COSC-2) could help to identify resistive structures underneath the shallow alum shale cover in the central and eastern parts of the profile. The inversion model from the determinant impedance in Fig. 13(a) with two additional resistive layers at ~20 and 38 km along the profile (Fig. 14a) were used as the original model. These positions correspond to the locations proposed for COSC-2 by Juhlin *et al.* (2016). Forward responses were calculated with the same station locations and periods as the real data. Before inversion, 10 per cent of noise on apparent resistivity and 2.85° absolute noise on phase were added to the calculated forward responses. Three boreholes were assumed with one being COSC-1 and the other two being the two options for future borehole COSC-2 in the east intersecting the additional resistive layers. The resistivities of the original model were set as the input borehole data constraints. During the inversions, the weights for smoothness in the horizontal and vertical directions were set to 10 and 1, respectively. The original and inverse models that were retrieved without and with help of the borehole information are shown in Fig. 14. Although the data fit of Fig. 14(b) (rms = 1.006) is almost as good as that of Fig. 14(c) (rms = 1.004), the comparatively thin resistive units underneath a very conductive cover cannot be revealed from normal inversion of MT data without a priori borehole constraints (Fig. 14b). Therefore, in our study area, the structures in the MT inversion model at depth >2 km below the less than 1 km deep transition to a conductive unit are not very reliable. As apparent in Fig. 14(c), using constraints from a future borehole COSC-2, this problem could be resolved in the vicinity of the borehole, although the lateral extent of the effect is limited.

6 INTERPRETATION AND DISCUSSION

For comparison and interpretation, in Fig. 15, the CSP (Juhlin *et al.* 2016) is overlain on top of our preferred resistivity model from Fig. 13(a). Note that the resistivity model has been partly extended or squeezed in the horizontal direction to ensure that the projected locations of the MT stations match the corresponding CDP locations of the CSP. The semi-transparent and transparent areas of the resistivity model in Fig. 15 indicate where Schwalenberg *et al.*'s (2002) averaged sums of absolute normalized sensitivities (eq. 7 in Schwalenberg *et al.* 2002) have dropped
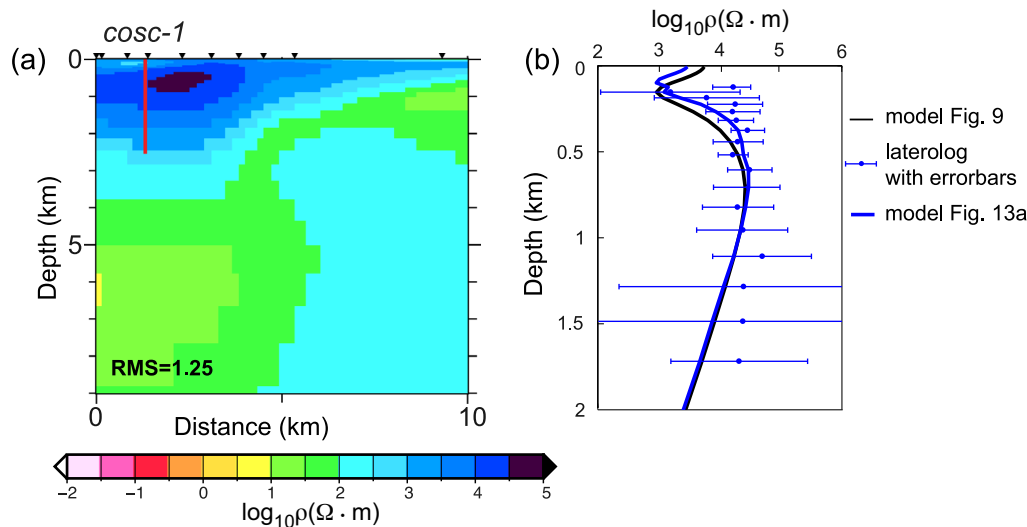
Figure 13. (a) 2-D resistivity model resulting from inversion of the MT determinant impedances using the depth-averaged deep laterolog of COSC-1 as borehole prior constraints. The resistivities of the 2-D inversion models in Figs 9 and 13(a) along the COSC-1 borehole are plotted in (b) together with the input borehole constraints and their standard deviations. Note that the deep laterolog is explained by the constrained inversion to within the estimated uncertainties and that the borehole log affects the 2-D resistivity model only in the immediate surrounding of the borehole.
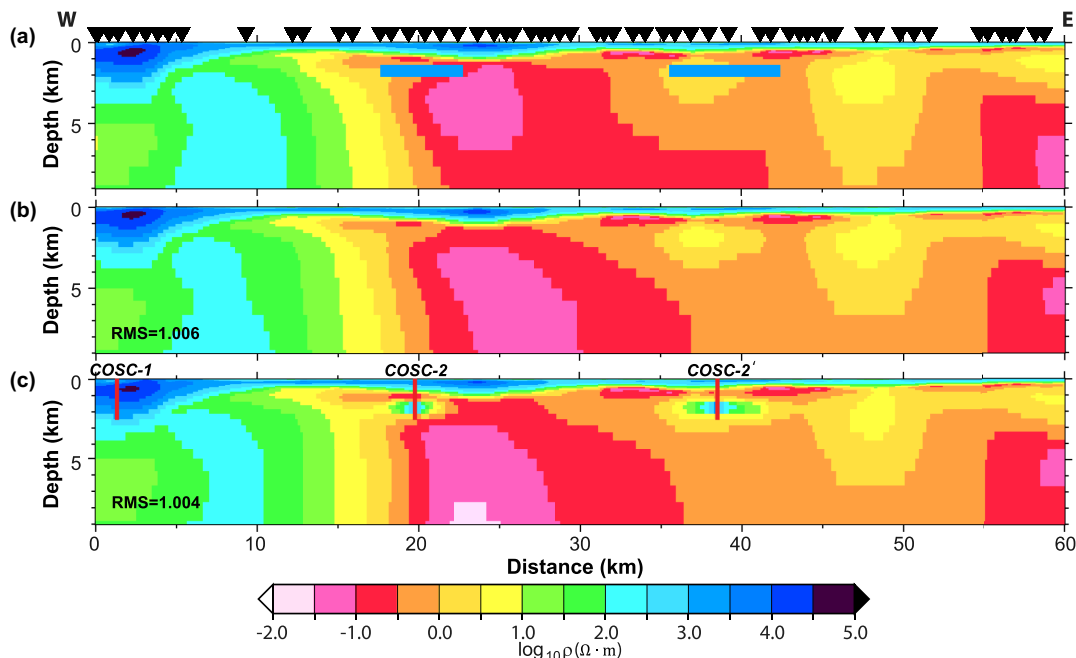

Figure 14. Synthetic test example with three borehole resistivity logs corresponding to COSC-1 and two possible locations for future borehole COSC-2 (marked by red lines): (a) true resistivity model (b) inverse model without borehole constraints and (c) inverse model with borehole logs as prior constraints. The true model is the resistivity model inverted from the real MT data and the depth-averaged deep laterolog of COSC-1 as prior constraints with additional elongated resistive units at 17.5–22.5 and 35.5–42 km along the profile.

below $10^{-4.5}$ and 10^{-5}, respectively. Since our 1-D inversion results revealed the >3 km deep eastern conductor to be a robust model feature and the upper part of this conductor has summed absolute sensitivities $>10^{-5}$ in the 2-D inversion model, we assume resistivities of cells with summed absolute sensitivities $>10^{-5}$ to be at least partly constrained by the data. Based on Fig. 15, the following interpretations of the robust features in the MT model are made together with the borehole resistivity and lithology information from COSC-1 (Fig. 5), the surface geologic map (Fig. 2) and near-surface resistivity information from the airborne VLF map (Fig. 3).

6.1 The western 10 km of the profile

In the western 10 km of our profile, strike and distortion analyses (Fig. 8) show a predominantly 3-D structure. The maximum penetration depth in this part of the profile computed using Schmucker's (1987) $\rho^*(z^*)$ method is >9 km. However, considering the 10^{-5} isoline of the scaled total sensitivities (Schwalenberg *et al.* 2002) suggests a more conservative maximum penetration depth of 8–9 km. The resistivity model consists of a resistor R1 (>1000 $\Omega \cdot$ m) lying on top of a relatively conductive structure (between 10 and 1000 $\Omega \cdot$ m).
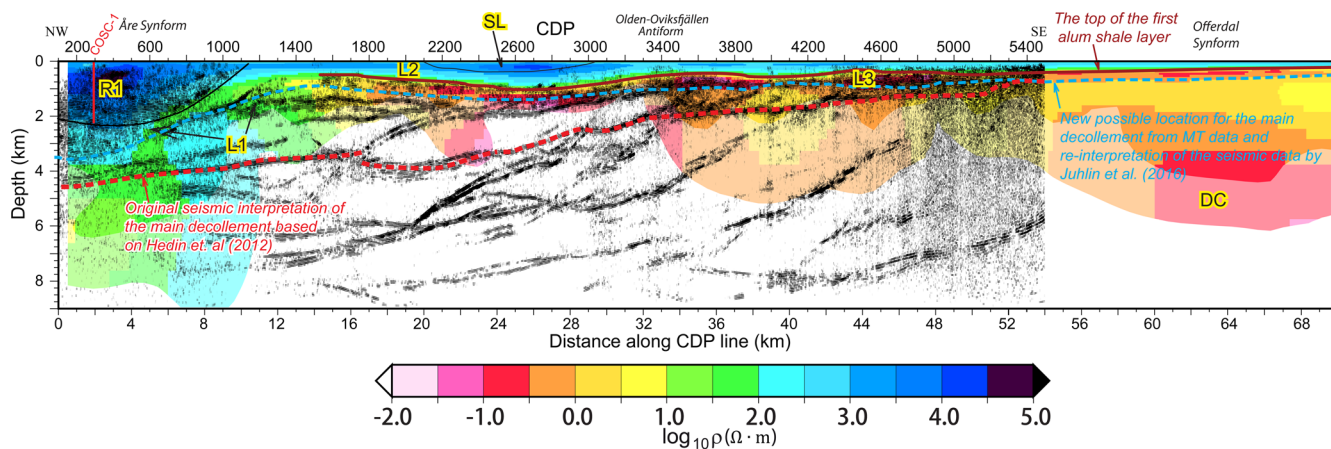
Figure 15. 2D resistivity model computed using the depth-averaged deep laterolog from COSC-1 as prior information (*cf.* Fig. 13a) overlain with CSP reflection image (Fig. 4) and possible locations of the décollement surface: R1 – resistor corresponding to Seve Nappe Complex, SL – Silurian turbidites, L1 – conductive unit underneath R1, L2 – resistive unit of Lower Allochthon, L3 – conductive alum shales, DC – deep conductor in Precambrian basement. The partly transparent area shows the places where scaled total sensitivities (Schwalenberg *et al.* 2002) of the MT model are between $10^{-4.5}$ and 10^{-5}. Areas of the model with scaled total sensitivities below 10^{-5} have been made entirely transparent (white), because they are poorly constrained by the data. The main décollement may be located either inside L1 and L3 (blue dashed line) or along the deep seismic reflection at 4.5 km depth underneath the western end of the profile (red dashed line). The dark red solid line indicates the boundary between units L2 and L3.

The location and shape of resistor R1 correlates well with the highly reflective feature in the seismic section. Compared with the surface geologic map (Fig. 2) and borehole lithology, this resistor is related to the Seve Nappe Complex. From both the MT inversion model and the reflection seismic section, the Seve Nappe Complex appears to extend down to ~2.7 km at its deepest position in the west and it thins out towards the east reaching a few hundred meters depth at ~10 km along the profile. In borehole COSC-1 (Fig. 5), at the western side of resistor R1, the Lower Seve Nappe Complex extends down to ~2350 m depth. Inside the Lower Seve Nappe Complex, between 1700 and ~2350 m, an increasing number of mylonite bands are observed, indicating increasing strain. In this depth interval, the borehole logging resistivities are high whereas the SP curve varies rapidly at very low values. At the bottom of the borehole, 10–20 m thick successions of metasandstones appear within a ~150 m thick interval, with decreasing resistivities and increasing SP values.

A relatively conductive layer L1 (between 10 and 100 $\Omega \cdot$ m) can be traced underneath resistor R1 with depths of ~2 and 1 km at distances of 5 and 10 km along the profile, respectively. Alum shale may constitute this conductive layer L1. Unfortunately, the MT data between 6 and 10 km along the profile had to be rejected because of strong noise effects from infrastructure in the vicinity of these stations. Hence, the relatively conductive layer L1 is not well constrained in the 2-D inversion models and it is uncertain whether alum shale occurs at these depths. 3-D inversion that includes the four (five before data editing) stations from the northern short profile (Fig. 2) may give better constraints on the distribution of alum shale underneath the Seve Nappe Complex.

6.2 The central and eastern parts of the profile

In the central and eastern parts of the profile, a boundary where resistivity drops rapidly from over 100 $\Omega \cdot$ m to less than 1 $\Omega \cdot$ m separates the structure into two parts: the top resistive layer L2 (100–10 000 $\Omega \cdot$ m) with 1 km as the maximum depth and the underlying conductive units (0.01–100 $\Omega \cdot$ m). As alum shales have

very low resistivity (<1 $\Omega \cdot$ m; Gee 1972), this boundary probably represents the top of a first alum shale layer L3.

6.2.1 The boundary between L2 and L3

The depth of the boundary between L2 and the underlying conductive units is well constrained by our MT data. The 2-D resistivity models inverted using different algorithms or from different impedances show similar depths to this boundary (Figs 15 and B1). Moreover, for five selected sites, the 1-D Marquardt-Levenberg inversion models in Figs 11 and 12 show the conductive layer at the same depth as in our 2-D inversion models. In Fig. 15, the boundary is undulating (indicated by solid red line), reaching depths of 300 m at the eastern end of the MT profile, 500 m at CDP 5050, 300 m at CDP 4450, 600 m at CDP 4000 and 400 m at CDP 3500. Further west, it sinks to 1100 m at CDP 2700 and then rises back to 600 m at CDP 1600. The shallower depth to the conductor at around CDP 3400 coincides with the Olden-Oviksfjällen Antiform. Compared with the CSP, the boundary correlates remarkably well with the first reflection in the seismic image. However, the top to the earliest reflection has its greatest depth at CDP 2950, while the resistivity boundary has its greatest depth at CDP 2700. This discrepancy may be due to the large lateral offset between the seismic and MT profiles between CDP 2850 and 3400. In this area, the seismic shot and receiver points are located to the southwest of the CSP line (Juhlin *et al.* 2016), while the MT stations are located to its northeast (Fig. 2).

6.2.2 The top resistive layer L2

As mentioned before, the thickness of the top resistive layer is very well constrained. Between 10 and 30 km along the profile, the resistivity of the layer is over 1000 $\Omega \cdot$ m and the thickness is between 500 m and 1 km, whereas in the eastern part of the profile (>30 km along the line), the resistivity decreases to between 100 and 1000 $\Omega \cdot$ m and the layer thins to less than 500 m. In the

very top, the seismic section is totally transparent between 10 and 30 km along the profile while towards the east it becomes more reflective. As discussed in the seismic interpretation by Hedin *et al*. (2012), homogeneous units of Ordovician and Silurian greywackes with very low internal contrasts of seismic impedance are the most likely candidates for explaining this top layer, which shows to be resistive in the MT inversion models. Within layer L2, the highest resistivities occur around 26 km along the profile, where Silurian formations are expected from the geologic map in Fig. 2, indicating that Silurian greywackes are more resistive than Ordovician rocks, which is also supported by the VLF data.

6.2.3 *The underlying conductive units*

Underneath the top resistive layer L2, the lithological units become very conductive ($<10 \, \Omega \cdot m$) especially for the structure between 20 and 30 km along the profile ($<0.1 \, \Omega \cdot m$). However, in most of this area, the MT model loses resolution because at many sites the transfer functions had to be cut at a period of 0.1 s. For these sites, the approximate values of the depth of penetration, as estimated using Schmucker's depth z^* and the 10^{-5} isoline of the scaled total sensitivities (Schwalenberg *et al*. 2002), are about 2 and 1.9 km, respectively. Since we only want to interpret robust features of the model, we do not consider the conductivity structures below 2 km depth in this part of the profile (transparent area in Fig. 15).

As discussed previously, the top of the alum shale unit L3 is well constrained. Between 20 and 33 km along the profile, the high conductivities of this layer smear down to several kilometres, which is a geologically implausible thickness for the alum shale. As the resistivity model is not well constrained below 1.9 km depth in this area, the thickness of the alum shale layer L3 and the existence of deeper alum shale layers are uncertain. However, in the eastern part of the profile (>34 km), the maximal penetration depth is $\sim$5 km and the thickness of L3 is depicted as 300–500 m. A similarly thin conductive layer is represented in the other resistivity models obtained using TE and TM mode impedances (Figs B1c, d and e). In support of our interpretation, alum shale with very low resistivity ($<1 \, \Omega \cdot m$) and thickness of tens to hundreds of meters was mapped at the Caledonian front (Gee 1972). Under the thin conductive layer, the structure becomes more resistive (between 1 and $10 \, \Omega \cdot m$), but not as resistive as L2. Underneath the easternmost 5 km of the profile, a second conductor ($<1 \, \Omega \cdot m$) is encountered deep (>3 km) inside the assumed Precambrian basement. In Fig. 12, we have demonstrated the necessity of including this deep conductor to explain our data using 1-D inversion. This deep conductor may represent a graphite schist unit inside the Precambrian basement (personal communication David G. Gee).

6.3 The main décollement and COSC-2

Thrusting along the main décollement that generally separates the allochthons from the underlying autochthonous Proterozoic basement is believed to have been facilitated by alum shales. In the central and eastern parts of the profile in our resistivity models, the highly conductive ($<1 \, \Omega \cdot m$) unit L3 of 300–500 m thickness is encountered at a depth of less than 1 km, coincident with the shallowest reflections in the seismic section. This allows for two different, partly complementary interpretations.

Our first and preferred interpretation is that the upper part of L3 consists of imbricated alum shales of the Lower Allochthon and that the main décollement is associated with the lower part of layer L3 (Fig. 15). This interpretation receives strong support from the reflection seismic image presented by Juhlin *et al*. (2016), where the interpreted main décollement (blue dashed line in Fig. 15) is coincident with a laterally continuous seismic reflection and the immediately overlying seismic reflections resemble imbricated sedimentary units. In the central and eastern parts of the profile, the depth to the top of this alum shale layer L3 is well constrained. The top of L3 can be tracked to the west below the Seve Nappe Complex, if the conductive layers L1 and L3 are assumed to be the same unit. Compared with the resistivities of the alum shales in the central and eastern parts of the profile ($<1 \, \Omega \cdot m$), the resistivity of layer L1 appears a little too high ($10–100 \, \Omega \cdot m$) to be alum shale. However, the relatively conductive layer L1 could be replaced by a thinner but more conductive layer with the same data fit. Therefore, from the resistivity models, alum shale possibly occurs underneath the Lower Seve Nappe Complex, but neither the location nor the thickness is well constrained. This problem is left to be solved by future research. If this first interpretation is correct, the location of the second borehole COSC-2, planned to penetrate the main décollement and investigate the underlying Precambrian basement, can be placed anywhere in the central and eastern parts of the profile.

A second option is a deeper thrust zone (Fig. 15) that corresponds to the décollement in the original seismic interpretation of (Hedin *et al*. 2012). This associated reflections occur at a depth of 4.5 km at the western end of the profile and shallow to a depth of $\sim$2 km at a distance of 35 km (CDP 3600) and merge with the top reflection at around profile km 51 (CDP 5200). Following Juhlin *et al*. (2016), this postulated décollement would thus be associated with a seismic reflector that is much less laterally continuous than the one corresponding to the main décollement in the first interpretation. If these reflections would represent the main Caledonian décollement, the less than 1 km deep resistivity boundary between L2 and L3 and the very conductive layer L3 underneath this boundary consisting of alum shales would entirely pertain to the Lower Allochthon. Between the conductive layer L3 and a deeper conductive layer associated with the alum shales of the detachment horizon, the resistivity model should have other more resistive units of the Lower Allochthon associated with Ordovician limestones, Ordovician to Silurian greywackes and, possibly, quartzites. Such resistive units are not visible in our 2-D inversions models, which makes this the second interpretation unlikely, and/or the MT method is inherently unable to detect thin resistive layers between well-developed conductive layers.

Taking into account the cumulative geophysical evidence, both MT and reflection seismic data and interpretations strongly suggest a shallow main décollement that is hosted in the Cambrian Alum shales (blue line in Fig. 15) and which, in the seismic section, is represented by the prominent continuous reflector. The imbricates above this décollement involve alum shales and, thus, produce the comparatively thick conductor L3. It is likely that the Precambrian basement below the main décollement was involved in Caledonian and also earlier deformation. The less continuous reflections could represent a sole thrust to this basement deformation that, however, could also be located at both deeper and shallower levels. One of the criteria in planning the COSC-2 drill hole is to penetrate at least one, but possibly several shallow basement reflectors in order to study the relationship between thrust- and basement-tectonics across the main Caledonian décollement.

6.4 Comparison with previous MT research in this area

The previous MT research along the CCT reflection seismic profile conducted by Korja *et al*. (2008) covered a region adjacent to ours and was located 5–30 km farther to the north (Fig. 2). As mentioned above, the strike direction calculated by Korja *et al*. (2008) was 6° different from ours, which may be related to gradual changes in Precambrian bedrock geology. Our MT profile projects onto the CCT profile at about 50–100 km along the CCT profile. In this area, the previous 2-D MT resistivity model (Korja *et al*. 2008) showed a westward-dipping conductive layer with a well-defined upper boundary underlying a resistive layer, which is quite similar to our result. In Korja *et al*.'s (2008) model, the depth of the boundary is ~1 km in the east (at 100 km along the CCT profile) and deepens to 2 km at 70 km along the CCT profile and further to ~2.8 km in the west (at 50 km along the CCT profile). However, in the parts of our resistivity model that correspond to 70 and 100 km along the CCT profile, the transition to the highly conductive layer L3 occurs at ~1 km and 300 m, respectively. Moreover, between 85–100 km along the CCT profile, Korja *et al*.'s (2008) boundary also correlates relatively well with a set of seismic reflectors, although not as well as in our model. In Korja *et al*.'s (2008) interpretation, the Caledonian allochthons are supposed to form the resistive layer and the Lower Allochthon is more conductive than the Middle and Upper Allochthons. This is consistent with our results where the Seve Nappe (Middle Allochthon) is more resistive than the Silurian and Ordovician greywackes (Lower Allochthons). Similar to our result, the conductive layer in Korja *et al*.'s (2008) model is interpreted as a mixture of alum shales and resistive basement rocks.

Overall, our results agree well with previous MT research, but offer additional details with much higher resolution.

7 CONCLUSIONS

We present new broad-band MT data along a 60-km-long profile together with resistivity logs from the in-profile borehole, COSC-1, in Jämtland, central Sweden. The MT data have been processed, analysed and carefully inverted with various 2-D approaches. The robustness and reliability of the obtained models were tested through 1-D inversions of the full impedance tensor or determinant impedance of selected MT sites in key areas of the profile and through sensitivity analysis. Additionally, prior information from the resistivity logging of the COSC-1 borehole has been used to constrain the resistivity model. Although in this particular application the model was not strongly affected by the borehole constraints, using a synthetic example, we have demonstrated the great potential of this technique to render a significantly improved resistivity model in other areas along the profile that are not so well constrained by the MT data (i.e. underneath the shallow alum shale cover at the planned borehole COSC-2).

Together with the COSC-1 borehole information, the CSP reflection image, a surface geological map and the airborne VLF map, we discussed and interpreted the obtained 2-D MT resistivity model constrained by the deep laterolog data. The Lower Seve Nappe is very resistive and highly reflective. Its shape and location are well constrained from both the resistivity model and the seismic section. The underlying Lower Allochthons are more conductive than the Lower Seve Nappe. Two alternative and partly complementary interpretations are presented. In the suggestion based on the original interpretation of the reflection seismic image (Hedin *et al*. 2012), a major deformation zone is located at a depth of 4.5 km at the western end of the profile and reaches a depth of roughly 1 km at 40 km along the profile. However, our resistivity models and the interpretation of the reflection seismic image by Juhlin *et al*. (2016) indicate that another interpretation is more plausible. In this new interpretation, the conductive alum shales associated with the main décollement are already encountered at a depth of 1000–300 m in the central and eastern parts of the profile, the main décollement is interpreted to coincide with a laterally continuous seismic reflection in the lower part of this conductive alum shale unit, and the upper part of this conductive unit carries a seismic signature strongly indicative of imbricated sedimentary units.

In our 2-D MT inversions, the impedance tensors with periods greater than 1 s for six sites are not used as their phases are out of quadrant. These phases cannot be explained using an isotropic 2-D model and probably represent 3-D effects in the data. Moreover, the strike and distortion analyses show a strong 3-D structure in the western 10 km (Fig. 8), where we have also disregarded further MT data collected along a northern branch of the profile. Therefore, our next step is to perform 3-D inversion of the MT data to make full use of the data and to provide a 3D resistivity model that helps us to improve our geological understanding of western Jämtland, especially around borehole COSC-1. Furthermore, performing 3-D inversion of our MT data collected along the CSP profile, the MT data previously collected along the CCT profile (Korja *et al*. 2008; green diamonds in Fig. 2) and future MT data to be collected between the CSP and CCT profiles would help us to understand the differences between the existing 2-D resistivity models along the CSP and CCT profiles.

The algorithm proposed for constrained MT inversion using borehole logs as prior information works well. Our more theoretical consideration of normal resistivity logs and laterologs, the analysis of the logs recorded in COSC-1 and the inversion results using these logs as prior constraints suggest that averaged deep laterolog resistivities from COSC-1 can be meaningfully included as prior constraints, whereas long normal resistivities should be used with more caution in highly resistive environments. Although constraints from COSC-1 only slightly improve the MT resistivity model in the vicinity of the borehole, our synthetic modelling studies suggest that constraints from a future borehole COSC-2 can provide our MT resistivity model with much better resolution of the structures underlying the top conductive layer. With borehole information from COSC-2, several problems would be resolved, for example, whether resistors related to imbrication exist in the highly conductive layer L3. Further in our synthetic modelling examples, the strong weight on the horizontal smoothness leads the prior information from a COSC-2 resistivity log to be spread predominantly in a horizontal direction to distances of ~2 km from the borehole. In general, in what directions and to what distances from a borehole prior information from resistivity logs will be carried in the model will depend on the applied model regularization (smoothness constraints) and to what extent MT data from stations in the vicinity of the borehole are compatible with the prior information.

Since the borehole COSC-2 will only be drilled to 2.5 km depth, the resistivity structure and possible distribution of alum shales below this depth will still be difficult to study. Although most of the deep reflections from the seismic section do not have any apparent correspondence in the resistivity models, some of the deeper reflectors underneath the transition to conductive alum shale at 1 km depth correlate with contrasts in resistivity. Thus, performing MT inversions with the reflection seismic images as prior information has the potential to improve the resistivity models and in turn our geological interpretation.

ACKNOWLEDGEMENTS

REFERENCES

Agustsson, K., 1986. A magnetotelluric pilot study in the Scandes, *Geol. Föreningen i Stock. Förhandlingar,* **108,** 258–261.

Anderson, B.I., 2001. Modeling and inversion methods for the interpretation of resistivity logging tool response, *PhD thesis,* Delft University of Technology, The Netherlands.

Andersson, A., Dahlman, B., Gee, D.G. & Snäll, S., 1985. The Scandinavian Alum Shales, Sveriges geologiska undersökning, Uppsala.

Bahr, K., 1991. Geological noise in magnetotelluric data: a classification of distortion types, *Phys. Earth planet. Inter.,* **66,** 24–38.

Bastani, M., Savvaidis, A., Pedersen, L.B. & Kalscheuer, T., 2011. CSRMT measurements in the frequency range of 1–250 kHz to map a normal fault in the Volvi basin, Greece, *J. appl. Geophys.,* **75,** 180–195.

Becken, M. & Pedersen, L.B., 2003. Transformation of VLF anomaly maps into apparent resistivity and phase, *Geophysics,* **68,** 497–505.

Berdichevsky, M.N. & Dmitriev, V.I., 2008. *Models and Methods of Magnetotellurics,* Springer.

Bylund, G., Gee, D.G., Gorbatschev, R., Ramberg, H., Stephansson, O., Strömberg, A., Werner, S. & Zachrisson, E., 1976. The Caledonian Research Project (CRP): A Swedish contribution to the International Geodynamics Project (IGP), *Geol. Föreningen i Stock. Förhandlingar,* **98,** 99–110.

Cagniard, L., 1953. Basic theory of the magnetotelluric method of geophysical prospecting, *Geophysics,* **18,** 605–635.

Caldwell, T.G., Bibby, H.M. & Brown, C., 2004. The magnetotelluric phase tensor, *Geophys. J. Int.,* **158,** 457–469.

Chave, A.D. & Jones, A.G., 2012. *The Magnetotelluric Method: Theory and Practice,* Cambridge Univ. Press.

Cherevatova, M. *et al.*, 2015. Magnetotelluric array data analysis from northwest Fennoscandia, *Tectonophysics,* **653,** 1–19.

Corfu, F., Andersen, T.B. & Gasser, D., 2014. The Scandinavian Caledonides: main features, conceptual advances and critical questions, *Geol. Soc. Lond., Spec. Publ.,* **390,** doi:10.1144/SP390.25.

Dewey, J.F., 1969. Evolution of the appalachian/caledonian orogen, *Nature,* **222,** 124–129.

Dyrelius, D., 1980. Aeromagnetic interpretation in a geotraverse area across the central Scandinavian Caledonides, *Geol. Föreningen i Stock. Förhandlingar,* **102,** 421–438.

Dyrelius, D., 1986. Gravity and magnetics in the central Scandes, *Geol. Föreningen i Stock. Förhandlingar,* **108,** 278–280.

Ellis, D.V. & Singer, J.M., 2007. *Well Logging for Earth Scientists,* Springer.

Elming, S.Å., 1980. Density and magnetic properties of rocks in the Caledonides of Jämtland, Sweden, *Geol. Föreningen i Stock. Förhandlingar,* **102,** 439–453.

Gamble, T.D., Goubau, W.M. & Clarke, J., 1979. Magnetotellurics with a remote magnetic reference, *Geophysics,* **44,** 53–68.

Gee, D.G., 1972. The regional geological context of the Tåsjö uranium project, Caledonian front, Central Sweden. Stockholm.

Gee, D.G. & Sturt, B.A. (eds), 1985. *The Caledonide Orogen: Scandinavia and Related Areas,* John Wiley and Sons Ltd.

Gee, D.G., Guezou, J.-C., Roberts, D. & Wolff, F.C., 1985. The central-southern part of the Scandinavian Caledonides, in *The Caledonide Orogen: Scandinavia and Related Areas, The Caledonide Orogen: Scandinavia and Related Areas*, pp. 109–133, eds Gee, D.G. & Sturt, B.A., John Wiley and Sons Ltd.

Gee, D.G., Fossen, H., Henriksen, N. & Higgins, A.K., 2008. From the Early Paleozoic Platforms of Baltica and Laurentia to the Caledonide Orogen of Scandinavia and Greenland, *Episodes,* **31,** 44–51.

Gee, D.G., Juhlin, C., Pascal, C. & Robinson, P., 2010. Collisional Orogeny in the Scandinavian Caledonides (COSC), *GFF,* **132,** 29–44.

Groom, R.W. & Bailey, R.C., 1989. Decomposition of magnetotelluric impedance tensors in the presence of local three-dimensional galvanic distortion, *J. geophys. Res.,* **94,** 1913–1925.

Hedin, P., Juhlin, C. & Gee, D.G., 2012. Seismic imaging of the Scandinavian Caledonides to define ICDP drilling sites, *Tectonophysics,* **554–557,** 30–41.

Hedin, P., Malehmir, A., Gee, D.G., Juhlin, C. & Dyrelius, D., 2014. 3D interpretation by integrating seismic and potential field data in the vicinity of the proposed COSC-1 drill site, central Swedish Caledonides, *Geol. Soc. Lond., Spec. Publ.,* **390,** 301–319.

Hedin, P. *et al.*, 2016. 3D reflection seismic imaging at the 2.5 km deep COSC-1 scientific borehole, central Scandinavian Caledonides, *Tectonophysics,* **689,** 40–55.

Hurich, C.A., Palm, H., Dyrelius, D. & Kristoffersen, Y., 1989. Deformation of the Baltic continental crust during Caledonide intracontinental subduction: views from seismic reflection data, *Geology,* **17,** 423–425.

Juhlin, C., Hedin, P., Gee, D.G., Lorenz, H., Kalscheuer, T. & Yan, P., 2016. Seismic imaging in the eastern Scandinavian Caledonides: siting the 2.5 km deep COSC-2 borehole, central Sweden, *Solid Earth,* **7,** 769–787.

Juhojuntti, N., Juhlin, C. & Dyrelius, D., 2001. Crustal reflectivity underneath the Central Scandinavian Caledonides, *Tectonophysics,* **334,** 191–210.

Kalscheuer, T., García Juanatey, M.A., Meqbel, N. & Pedersen, L.B., 2010. Non-linear model error and resolution properties from two-dimensional single and joint inversions of direct current resistivity and radiomagnetotelluric data, *Geophys. J. Int.,* **182,** 1174–1188.

Kalscheuer, T., Hübert, J., Kuvshinov, A., Lochbühler, T. & Pedersen, L.B., 2012. A hybrid regularization scheme for the inversion of magnetotelluric data from natural and controlled sources to layer and distortion parameters, *Geophysics,* **77,** E301–E315.

Kalscheuer, T. *et al.*, 2015. Joint inversions of three types of electromagnetic data explicitly constrained by seismic observations: results from the central Okavango Delta, Botswana, *Geophys. J. Int.,* **202,** 1429–1452.

Klonowska, I., Janák, M., Majka, J., Froitzheim, N. & Gee, D.G., 2015. The UHP metamorphic Seve Nappe Complex of the Swedish Caledonides—a new occurrence of the microdiamond-bearing gneisses and their exhumation, in *Geophysical Research Abstracts 17,* EGU2015-11609.

Korja, T., Smirnov, M., Pedersen, L.B. & Gharibi, M., 2008. Structure of the Central Scandinavian Caledonides and the underlying Precambrian basement, new constraints from magnetotellurics, *Geophys. J. Int.,* **175,** 55–69.

Lorenz, H., Gee, D. & Juhlin, C., 2011. The scandinavian caledonides—scientific drilling at mid-crustal level in a palaeozoic major collisional orogen, *Sci. Drill.,* **11,** 60–63.

Lorenz, H. *et al.*, 2015a. COSC-1 – drilling of a subduction-related allochthon in the Palaeozoic Caledonide orogen of Scandinavia, *Sci. Drill.,* **19,** 1–11.

Lorenz, H. *et al.*, 2015b. Operational Report about Phase 1 of the Collisional Orogeny in the Scandinavian Caledonides scientific drilling project (COSC-1), *GFZ Ger. Res. Cent. Geosci.,* **55,** doi:10.2312/ICDP.2015.002.

Majka, J., Rosén, Å., Janák, M., Froitzheim, N., Klonowska, I., Manecki, M., Sasinková, V. & Yoshida, K., 2014. Microdiamond discovered in the Seve Nappe (Scandinavian Caledonides) and its exhumation by the "vacuum-cleaner" mechanism, *Geology,* **42**(12), 1107–1110.

McNeill, J. & Labson, V., 1991. Geological mapping using VLF radio fields, in *Electromagnetic Methods in Applied Geophysics, Investigations in Geophysics*, pp. 521–640, Society of Exploration Geophysicists.

Ory, J. & Pratt, R.G., 1995. Are our parameter estimators biased? The significance of finte-difference regularization operators, *Inverse Probl.,* **11**, 397–424.

Palm, H., 1984. Time-delay interpretation of seismic refraction data in the Caledonian front, Jämtland, central Scandinavian Caledonides, *Geol. Föreningen i Stock. Förhandlingar,* **106**, 1–14.

Palm, H., Gee, D., Dyrelius, D. & Björklund, L., 1991. A Reflection seismic image of Caledonian structure in central Sweden. Sveriges geologiska undersökning, Uppsala.

Pedersen, L.B. & Engels, M., 2005. Routine 2D inversion of magnetotelluric data using the determinant of the impedance tensor, *Geophysics,* **70**, G33–G41.

Pedersen, L.B., Juhlin, C. & Rasmussen, T.M., 1992. Electric resistivity in the Gravberg-1 Deep Well, Sweden, *J. geophys. Res.,* **97**, 9171–9182.

Robinson, E.S. & Çoruh, C., 1988. *Basic Exploration Geophysics,* Wiley.

Schmucker, U., 1987. Substitute conductors for electromagnetic response estimates, *Pure appl. Geophys.,* **125**, 341–367.

Schwalenberg, K., Rath, V. & Haak, V., 2002. Sensitivity studies applied to a two-dimensional resistivity model from the Central Andes, *Geophys. J. Int.,* **150**, 673–686.

Sharma, S.P., Biswas, A. & Baranwal, V.C., 2014. Very low-frequency electromagnetic method: a shallow subsurface investigation technique for geophysical applications, in *Recent Trends in Modelling of Environmental Contaminants SE - 5*, pp. 119–141, ed. Sengupta, D., Springer.

Smirnov, M., 2003. Magnetotelluric data processing with a robust statistical procedure having a high breakdown point, *Geophys. J. Int.,* **152**, 1–7.

Smirnov, M.Y. & Pedersen, L.B., 2009. Magnetotelluric measurements across the Sorgenfrei-Tornquist Zone in southern Sweden and Denmark, *Geophys. J. Int.,* **176**, 443–456.

Strömberg, A., Karis, L., Zachrisson, E., Sjöstrand, T., Skoglund, R., Lundegårdh, P.H. & Gorbatschev, R., 1984. *Berggrundskarta över Jämtlands län utom förutvarande Fjällsjö kommun, scale 1:200 000* Sveriges Geologiska Undersökning (SGU), Uppsala.

Telford, W.M., Geldart, L.P. & Sheriff, R.E., 1990. *Applied Geophysics, Monograph Series,* Cambridge Univ. Press.

Tikhonov, A.N., 1950. On determining electrical characteristics of the deep layers of the Earth's crust, *Doklady,* **73**, 295–297.

Ulugergerli, E.U., 2011. Two dimensional combined inversion of short- and long-normal dc resistivity well log data, *J. appl. Geophys.,* **73**, 130–138.

Wannamaker, P.E., Hohmannl, G.W. & Ward, S.H., 1984. Magnetotelluric responses of three-dimensional bodies layered earths, *Explor. Geophys.,* **15**(3):190–191.

Wiese, H., 1962. Geomagnetische Tiefentellurik Tell I: die elektrische Leitfähigkeit der Erdkruste und des oberen Erdmantels, *Pure appl. Geophys.,* **52**, 83–103.

Zhang, P., Roberts, R. & Pedersen, L., 1987. Magnetotelluric strike rules, *Geophysics,* **52**, 267–278.

APPENDIX A: CONSTRAINED INVERSION ALGORITHM USING BOREHOLE DATA

To apply borehole resistivity data as constraints in Kalscheuer *et al.*'s (2010) inversion schemes, a term

$$\alpha Q_{BH}\left[\mathbf{m}_{k+1}\right] = \alpha(\mathbf{m}_{k+1} - \mathbf{m}_{bh})^{\mathrm{T}} \mathbf{W}_{\mathrm{bh}}^{\mathrm{T}} \mathbf{W}_{bh} \left(\mathbf{m}_{k+1} - \mathbf{m}_{bh}\right) \quad (A1)$$

is added to the cost functional U^{lin} in eq. (A4) in Kalscheuer *et al.* (2010).

Here, α is the weighting for the term Q_{BH} and is assigned a fixed value determined with initial test inversions. $\mathbf{m}_{k+1}$ is the inversion model to be solved for in iteration k + 1 and $\mathbf{m}_{bh}$ is the borehole resistivity log. $\mathbf{W}_{bh}$ is the weighting matrix for borehole data and is diagonal with non-zero diagonals only where model cells coincide with the borehole. When applying real borehole logging data as borehole constraints, the averaged resistivity log within each model cell is used as $\mathbf{m}_{bh}$, and the non-zero diagonals in $\mathbf{W}_{bh}$ are reciprocals of the standard deviations of borehole resistivities within each cell.

By setting the gradient $\nabla_{\mathbf{m}_{k+1}} U^{\mathrm{lin}} = 0$, the minimum of the modified cost functional (modified eq. A4 in Kalscheuer *et al*. 2010) can be found and the corresponding solution for an Occam inversion is

$$\mathbf{m}_{k+1}\left(\lambda, \alpha\right) = \left(\mathbf{J}^{\mathrm{T}}\mathbf{W}_{\mathrm{d}}^{\mathrm{T}}\mathbf{W}_{\mathrm{d}}\mathbf{J} + \lambda\mathbf{W}_{\mathrm{m}}^{\mathrm{T}}\mathbf{W}_m + \alpha\mathbf{W}_{\mathrm{bh}}^{\mathrm{T}}\mathbf{W}_{bh}\right)^{-1}$$
$$\times \left(\mathbf{J}^{\mathrm{T}}\mathbf{W}_{\mathrm{d}}^{\mathrm{T}}\mathbf{W}_{\mathrm{d}}\hat{\mathbf{d}}_k + \alpha\mathbf{W}_{\mathrm{bh}}^{\mathrm{T}}\mathbf{W}_{bh}\left(\mathbf{m}_{bh} - \mathbf{m}_r\right)\right) + \mathbf{m}_r,$$
$$(A2)$$

where

$$\hat{\mathbf{d}}_k = \mathbf{d} - \mathbf{F}\left[\mathbf{m}_k\right] - \mathbf{J}\left(\mathbf{m}_k - \mathbf{m}_r\right), \quad (A3)$$

and $\mathbf{F}\left[\mathbf{m}\right] = (F_1, \ldots, F_N)^{\mathrm{T}}$ is a set of N forward responses for M model parameters; $\mathbf{d} = (d_1, \ldots, d_N)^{\mathrm{T}}$ is a set of N field measurements; $\mathbf{J} = \{\frac{\partial F_i[\mathbf{m}]}{\partial m_j}\}_{\mathbf{m}=\mathbf{m}_k}$ is the Jacobian matrix of partial derivatives of $\mathbf{F}$ with respect to the model of iteration k; $\mathbf{W}_{\mathrm{d}}$ and $\mathbf{W}_m$ are weighting matrices of data and model containing reciprocal data uncertainties and smoothness constraints, respectively; $\mathbf{m}_r$ is the reference model; λ is the Lagrange multiplier and the superscript T indicates transposition.

Adding additional Marquardt-Levenberg damping to stabilize the model finding process (Kalscheuer *et al*. 2010), the solution is

$$\mathbf{m}_{k+1}\left(\lambda, \epsilon, \alpha\right) = \left(\mathbf{J}^{\mathrm{T}}\mathbf{W}_{\mathrm{d}}^{\mathrm{T}}\mathbf{W}_{\mathrm{d}}\mathbf{J} + \lambda\mathbf{W}_{\mathrm{m}}^{\mathrm{T}}\mathbf{W}_m + \epsilon\mathbf{I} + \alpha\mathbf{W}_{\mathrm{bh}}^{\mathrm{T}}\mathbf{W}_{bh}\right)^{-1}$$
$$\times \left(\mathbf{J}^{\mathrm{T}}\mathbf{W}_{\mathrm{d}}^{\mathrm{T}}\mathbf{W}_{\mathrm{d}}\hat{\mathbf{d}}_k + \epsilon\left(\mathbf{m}_k - \mathbf{m}_r\right)\right.$$
$$\left. + \alpha\mathbf{W}_{\mathrm{bh}}^{\mathrm{T}}\mathbf{W}_{bh}\left(\mathbf{m}_{bh} - \mathbf{m}_r\right)\right) + \mathbf{m}_r, \quad (A4)$$

where ϵ is the damping factor.

Since logging resistivities are apparent resistivities and not the true resistivities of the Earth, one may argue that the borehole logs need to be formally inverted for model resistivities and that such model resistivities should be included as prior constraints in the inversion of MT data. However, such a procedure would imply the following difficulties and limitations. First, in COSC-1 normal log and laterolog resistivities were logged every centimetre and decimetre, respectively, over a depth range of ∼2400 m, leading to 240 000 and 24 000 measurement locations. Even after resampling to one measurement location per tool length, that is one measurement point every 2.2 m for the dual laterolog tool, and allowing for 2 cells between abutting measurement positions, this would require about 2300 model cells in the vertical direction. To account for the borehole fluid and invasion zone using 3-D inversion, additional cells in both horizontal directions would be required, making the inversion problem difficult to handle in practice. Second, since it can be assumed that the MT data offer very limited sensitivity to the borehole and a possible invasion zone, one would have to extract the part of the model that is unaffected by the borehole for usage as prior constraints. Third, the resistivity model inverted from the borehole logs would still have to be averaged over the heights of the cells in the MT inversion model. Given the size of a hypothetical inversion model for borehole logging data and the size of our 2-D inversion model for MT data, it is also clear that a joint inversion of

borehole logging and MT data is infeasible. Hence, we have chosen a practical compromise and selected the apparent resistivities from logging averaged over the heights of the 2-D MT model cells as prior constraints.

APPENDIX B: OTHER 2D MT INVERSION MODELS USING DIFFERENT ALGORITHMS OR DATASETS

For the TM mode impedances, 10 per cent relative error and 2.85° absolute error were set as the lowest uncertainties for the apparent resistivities and phases, respectively. In contrast, for TE mode impedances, the lowest uncertainty for the apparent resistivity was set to 30 per cent relative error to decrease the effect of static shifts whereas the uncertainty floor for the phases was the same as for the TM mode impedances.

Three different inversion approaches were tested:

I. using a homogeneous half-space starting model and an Occam scheme;

II. using a homogeneous half-space starting model and a damped Occam scheme;

III. using the model retrieved in approach I as the starting model and a damped Occam scheme.

Our tests on the determinant data show that the Occam inversion scheme used in approach I (Fig. B1a, rms = 1.64) has convergence problems during the last iterations and the damped Occam scheme used in approaches II (Fig. B1b, rms = 1.29) and III (Fig. 9, rms = 1.26) avoids these using additional Marquardt-Levenberg damping. Since approach III generates a smooth model while fitting the data well (Fig. 9), this inversion strategy is recommended and also applied to the TE mode and TM mode datasets. Nevertheless, the models using approach II (Fig. B1b) and approach III (Fig. 9) look quite similar.

Figs B1(c), (d) and (e) show the inversion models for TE, TM and TE + TM mode impedances, using approach III; all of these models have significantly higher rms misfits than the determinant impedance model (Fig. 9). The responses of the TE inversion model in Fig. B1(c), and TM inversion model in Fig. B1(d) for 8 sites are plotted as red and blue lines in Fig. 6, respectively.
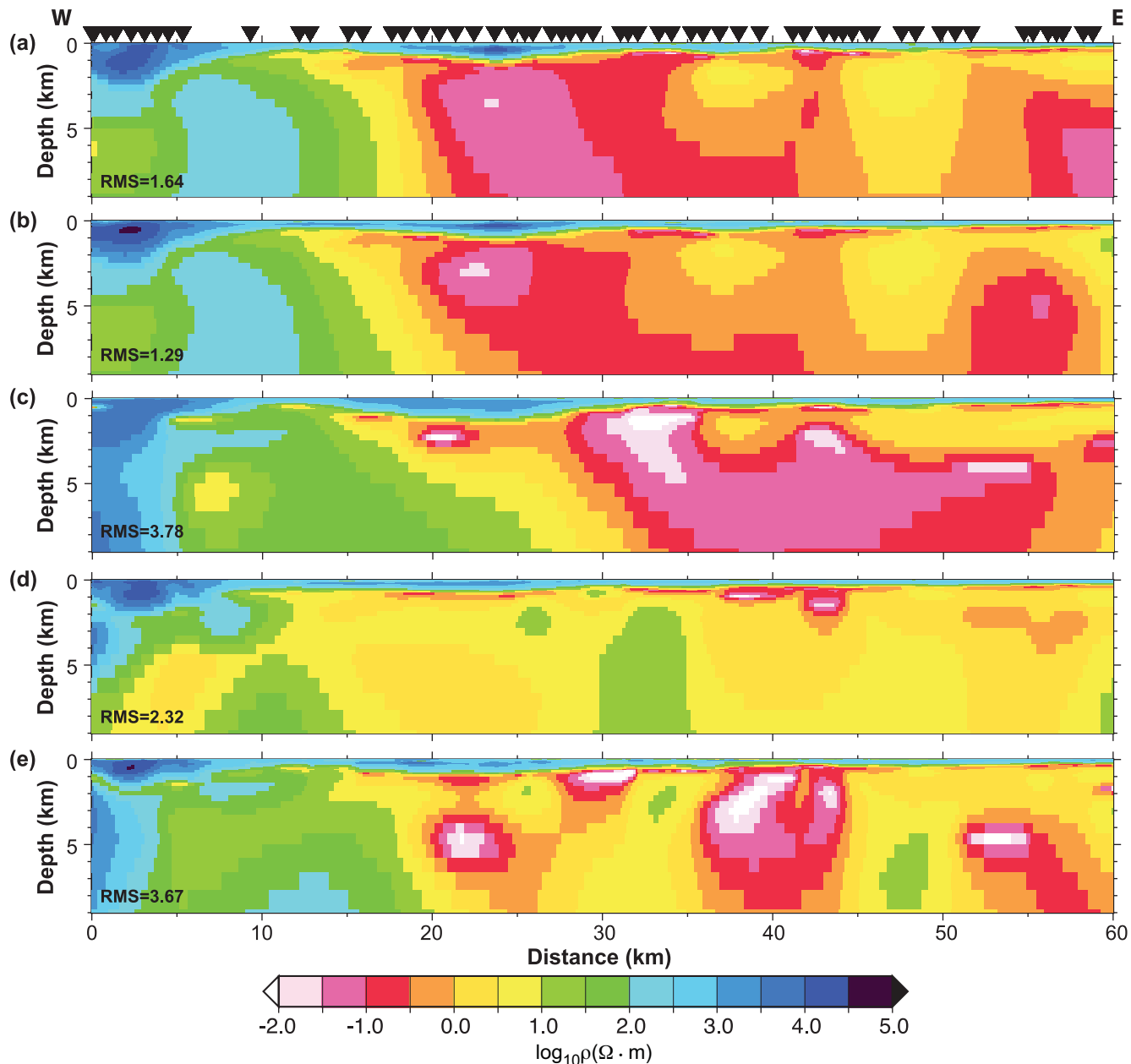
Figure B1. 2-D resistivity inversion models: (a) from the determinant impedances using an Occam scheme (approach I; see text for details); (b) from the determinant impedances using a damped Occam scheme (approach II); (c) from TE mode impedances; (d) from TM mode impedances; (e) from TE+TM mode impedances. The inversions leading to the models in (c), (d) and (e) used the same approach as for the model in Fig. 9, that is approach III.